



A Multi-Technology Analysis of the 2017 North Korean Nuclear Test

Peter Gaebler¹, Lars Ceranna¹, Nima Nooshiri², Andreas Barth³, Simone Cesca², Michaela Frei¹, Ilona Grünberg¹, Gernot Hartmann¹, Karl Koch¹, Christoph Pilger¹, J. Ole Ross¹, and Torsten Dahm²

¹ BGR, Federal Institute for Geosciences and Natural Resources, Hannover, Germany

² GFZ, German Research Centre for Geosciences, Potsdam, Germany

³ KIT, Karlsruhe Institute of Technology, Karlsruhe, Germany

Correspondence: Peter Gaebler (peter.gaebler@bgr.de), Stilleweg 2, 30655 Hannover, Germany

Abstract. On September 3rd 2017 official channels of the Democratic People's Republic of Korea announced the successful test of a thermonuclear device. Only seconds to minutes after the alleged nuclear explosion at the Punggye-ri nuclear test site in the mountainous region in the country's northeast at 03:30:02 (UTC) hundreds of seismic stations distributed all around the globe picked up strong and distinct signals associated with an explosion. Different seismological agencies reported body wave magnitudes of well above 6.0, consequently estimating the explosive yield of the device in the order of hundreds of kilotons TNT equivalent. The 2017 event can therefore be assessed being multiple times larger in energy than the two preceding events in January and September 2016.

This study provides a multi-technology analysis of the 2017 North Korean event and its aftermath using a wide array of geophysical methods. Seismological investigations locate the event within the test site at a depth of approximately 0.8 km below surface. The radiation and generation of P- and S-wave energy in the source region is significantly influenced by the topography of the Mt. Mantap massif. Inversions for the full moment tensor of the main event reveal a dominant isotropic component accompanied by significant amounts of double couple and compensated linear vector dipole terms, confirming the explosive character of the event. Analysis of the source mechanism of an aftershock that occurred around eight minutes after the test in the direct vicinity suggest a cavity collapse. Measurements at seismic stations of the International Monitoring System result in a body wave magnitude of 6.2, which translates to an yield estimate of around 400 kilotons TNT equivalent. The explosive yield is possibly overestimated, since topography and depth phases both tend to enhance the peak amplitudes of teleseismic P-waves. Interferometric Synthetic-Aperture-Radar analysis using data from the ALOS-2 satellite reveal strong surface deformations in the epicenter region. Additional multispectral optical data from the Pleiades satellite show clear landslide activity at the test site. The strong surface deformations generated large acoustic pressure peaks, which were observed as infrasound signals with distinctive waveforms even in distances of 400 km. In the aftermath of the 2017 event atmospheric traces of the fission product ¹³³Xe have been detected at various locations in the wider region. While for ¹³³Xe measurements in September 2017 the Punggye-ri test site is disfavored as source by means of atmospheric transport modeling, detections in October 2017 at the International Monitoring System station RN58 in Russia indicate a potential delayed leakage of ¹³³Xe at the test site from the 2017 North Korean nuclear test.



Copyright statement. Authors retain the copyright of the article. Authors grant Copernicus Publications an irrevocable non-exclusive licence to publish the article electronically and in print format and to identify itself as the original publisher. Authors grant Copernicus Publications commercial rights to produce hardcopy volumes of the journal for sale to libraries and individuals. Authors grant any third party the right to use the article freely as long as its original authors and citation details are identified. The article is distributed under the Creative Commons Attribution 4.0 License. Unless otherwise stated, associated published material is distributed under the same licence.

1 Introduction

The Comprehensive Nuclear Test-Ban-Treaty (CTBT) and its associated entity, the Preparatory Commission for the CTBT organization (CTBTO), are dedicated to monitoring and banning nuclear explosions worldwide – underground, in water, in the atmosphere or in space. It was opened for signature in 1996 but will only enter into force after the 44 nuclear technology holders (states listed in the Annex 2 of the CTBT) will have signed and ratified the treaty. At the time of this study eight Annex 2 states are still missing ratification, including North Korea. To detect, locate and characterize nuclear explosions an International Monitoring System (IMS) was established by the CTBTO as part of a verification regime. The IMS features four different approaches for the monitoring of potential nuclear explosions. Three methods (seismology, infrasound and hydroacoustics) are attributed to waveform technologies and have the purpose of detecting, localizing and identifying suspicious events with an explosive source mechanism. The fourth approach features the monitoring of particulate radionuclides and noble gases in the atmosphere and potentially provides the unambiguous evidence of the nuclear character of an explosion. For further information on the CTBT, the IMS, and the German National Data Center the reader is referred to Pilger et al. (2017) or CTBTO (2018).

Since the first known nuclear test, carried out by the United States in 1945, more than 2000 confirmed nuclear explosion tests were conducted by China, France, Great Britain, India, North Korea, Pakistan, Russia and the United States. It is generally accepted that all six past explosions in North Korea between 2006 and 2017 have been nuclear underground tests. This study therefore refers to the events in North Korea as nuclear tests, even definite proof might be missing. North Korea is the only country breaking the de facto moratorium on nuclear tests. For detailed information on the first five North Korean tests see for example Hartmann et al. (2017).

All past North Korean nuclear tests were conducted at the Punggye-ri test site in the vicinity of Mt. Mantap in the northeastern part of the country. Following the geologic description of the test site area provided by Coblentz and Pabian (2015) and Pabian and Coblentz (2017), Mt. Mantap is made out of two distinct geologic formations. The core of the mountain consists of igneous basement rock of either diorite or granite, while the top is capped by a thin layer of basaltic lava flows. The basement crystalline rock and the top layer of Mt. Mantap are separated by a nearly horizontal sequence of volcanic deposits with a thickness of around 200 m. The origin of these deposits is suspected to be volcanic ash from Mt. Paektu, a volcano located around 100 km northeast. Due to their loose consolidation, the volcanic deposits are softer than the basement rock or the basaltic layer and are therefore more susceptible to erosion. Furthermore, the volcanic layer is more exposed to erosional scars and landslides due to its steeper slope. The erosion of the volcanic layer can cause the overlying basalt cap to break off at the scarp, which is visible



in larger piles below the volcanic layer where the slope of the mountain slightly decreases.

The official channels of North Korea announced the 2017 event as a successful test of a fusion bomb. This would be a major step in the nuclear program of North Korea. From a scientific point, therefore, the depth of the event, its strength in terms of radiated high- and low-frequency seismic energy, the contribution of possible faulting or slope instability processes, the near surface damage in the test area as well as the proof whether fission products are detected as atmospheric tracers are key questions to be answered. These questions are approached by an integrated study based on different seismological (Section 2), infrasound (Section 3), remote sensing (Section 4), radionuclide monitoring (Section 5), and modeling techniques which complement each other. As there is not easy concept to verify and characterize nuclear explosions, especially in a country where direct observations are difficult to assess, this study demonstrates and emphasizes the strength of an integrated multi-technology approach.

In this context, new methodical approaches are introduced to improve the depth estimate from teleseismic observations and to quantify uncertainties in the non-isotropic source component. Radionuclide monitoring demonstrates the importance of atmospheric transport modelling (ATM) to avoid over-interpretation of variations in ^{133}Xe concentrations. The seismological study retrieves an independent absolute location based on a combination between seismological and remote sensing data. The relative location between the six North Korean nuclear tests is obtained by means of waveform cross correlation time lag data. The event depth is estimated for the first time by a joint inversion of source time function (STF) and depth phase waveform modeling observed at small aperture, high-frequency arrays in teleseismic distances. A full waveform moment tensor inversion (MTI) is applied and compared to results of previous explosions on North Korea. The source time overshoot and peak amplitude is compared to traditional body wave magnitudes (m_b) estimates. Additionally, the effect of topography on peak amplitudes is estimated by 2D-waveform modeling to estimate the possible range of explosive yield. Infrasound observations and modeling is used to understand the earth-atmosphere coupling and the propagation of infrasound from the North Korean test site, The analysis of satellite based remote sensing data is important to improve the absolute location of shallow sources as well as to quantify the secondary mass movement effects at the surface. While radionuclide monitoring provides the only direct evidence of nuclear explosions, it is demonstrated by careful modeling how difficult it is to interpret such data and that early claims of causal anomalies have possibly been over-interpreted.

2 Seismological Investigations

2.1 Epicenter Location

The localization in the Reviewed Event Bulletin (REB) of the CTBTO International Data Center (IDC) uses 125 seismic stations of the IMS and results in an epicenter of 41.321°N and 129.035°E with an error ellipse area of 110 km^2 . This relatively high error is generated by the fact that only eight IMS stations are located at distances from 400 km up to 2100 km (see Figure 1a).

Figure 1



However, the incorporation of 25 additional seismic stations in regional distances cannot significantly improve the absolute location estimate, as the closest station MDJ is still 372 km away from the test site. Due to these large source-receiver distances a further improvement of the absolute location accuracy is limited. Nevertheless, relative location methods can be applied for a high precision localization of the events (Zhang and Wen, 2013; Zhao et al., 2014, 2016; Gibbons et al., 2017). In this study a relative location procedure based on the cross-correlation of seismograms from 33 regional seismic stations for the six North Korean tests is applied. Seismograms for the past North Korean events significantly vary between the stations, due to propagation paths from source to the surrounding stations at different distances and azimuths. However, the correlation of the seismograms of the six events for each individual station shows a good coherence between the corresponding signals with the Pn-phase being the most pronounced arrival in the waveforms. These signals are correlated for each individual station, which has recorded at least two North Korean nuclear tests. The cross-correlation between each pair of events is performed using normalization to 1.0 for the auto-correlation of each signal at zero lag. Maximum correlation values of 0.7 to 0.99 are obtained for stations up to 1100 km distance for the four tests in the years 2009, 2013 and 2016. Due to significant differences in explosive yield, and therefore different source time durations, the 2006 and 2017 test are slightly less correlated with the other tests. See Figure 2 for the complete results of the cross-correlation analysis.

Figure 2

Time lags of the maximum cross-correlation values are used to determine precise travel time differences with an accuracy in the order of the sampling rate. Pn-phase onset times of all tests are aligned to the onset at the closest station MDJ and fixed as relative start time for the estimation of the correlation time lags at the other stations. A double difference method (e.g. Waldhauser and Ellsworth, 2000) is applied to cross correlation time lags and results suggest that the last five events are located within a radius of 400 m, while the 2006 test is located around 2 km further to the east (see Figure 1b). The relative locations of the six tests can be associated to absolute coordinates as soon as the geographical coordinates of one of the tests are known. The geographic, absolute location of the January 2016 nuclear explosion is fixed by means of radar interferometry data to the location of the maximum surface deformation observed after the test (Hartmann et al., 2017; Wei, 2017). The absolute epicenter location of the 2017 test from relative location procedures is consequently determined to be 41.3007°N , 129.0728°E (Figure 1b).

2.2 Estimation of Hypocenter Depth and Seismic Moment

The source depth is needed to estimate the explosion process and strength of the seismic source. However, constraining the depth of a shallow source is difficult from regional and teleseismic data without a close epicentral station above the source. The analysis of the time lag of near-source, surface-reflected P-phases, so-called depth phases, can potentially help in such a case, because they only depend on the depth and the P-wave velocity in layer above the source. However, such a depth phase approach needs high-frequency waveforms above 1 Hz to resolve the onset of the depth phase, and may be difficult from single stations recordings if the signal to noise ratio (SNR) is poor at teleseismic distances. An approach uncommon for nuclear test



studies is used, which was established for the analysis of induced seismicity, where waveform beams are calculated at several small-aperture, short-period arrays to enhance the SNR (Figure 3a).

Figure 3

The beam waveforms represent a superposition of direct and reflected waves. The depth of the explosion is estimated by comparing observed and synthetic beam waveforms (Figure 3d), which are calculated for the best moment tensor solution, a common STF and varying depths. The source time is represented as a composition of multiple basis functions with unknown weighting coefficients, which are estimated in a least squares inversion with smoothing constraint (Figure 4). If $u(t)$ is the seismogram (beam) at the array with coordinates \mathbf{r}_r and from a seismic source with coordinates \mathbf{r}_s , the P-wave train (i.e. P-plus pP- plus sP-phase) at time t is represented by

$$u(t) = \{M_{jk}G_{j,k}(\mathbf{r}_s, \mathbf{r}_r, t)\} * m(t), \quad (1)$$

where $*$ is a time convolution and where the summation convention is applied. $G_{j,k}$ are the spatial derivatives of the Green's function, where the comma before index $_{,k}$ indicates a spatial derivative with respect to x_k . It is assumed that all moment tensor components M_{jk} have the same time dependency, which is described as normalized STF $m(t)$ with $m(t \rightarrow \infty) = 1$. The waveform of far-field displacement pulses are controlled by the time derivative of $m(t)$, which is declared as moment rate function $\dot{m}(t)$. The P-wave from an earthquake $\dot{m}(t)$ has a single-sided pulse. Since only the far-field wavefield is considered, the Green functions in (1) are replaced by far-field Green functions $G^{(ff)}$, and $m(t)$ is replaced by $\dot{m}(t)$. The inversion is setup for $\dot{m}(t)$ using a set of N time-shifted triangular basis functions $h_l(t)$ (Figure 4):

$$\dot{m}(t) = \sum_{l=1}^N \beta_l h_l(t), \quad (2)$$

where β_l is a weighting factor and each $h_l(t)$ satisfies $\int h_l(t) dt = 1$.

Figure 4

Hence, equation (1) is written as

$$u(t) = \{M_{jk}G_{j,k}^{(ff)}(t)\} * \begin{bmatrix} h_1(t) & h_2(t) & \dots & h_N(t) \end{bmatrix} \cdot \begin{bmatrix} \beta_1 \\ \beta_2 \\ \vdots \\ \beta_N \end{bmatrix}. \quad (3)$$

The convolution in (3) can be equated and written in discrete form, leading to an over-determined matrix system for unknown weighting factors to be solved in a least squares sense using the L_2 -norm (Dahm and Krüger, 2014). If more than one array is available, the equations are added to the coefficient matrix to realize a joint inversion. Additionally, the STF inversion is stabilized by using a regularization with a roughness matrix. The STF is inverted for every single trial depth. The length of the STF is constrained to 1.5 s, where 0.5 s are considered before the arrival of the P-wave. It should be noted that, with



shorter length of STF, the details of the STF with a complex structure are difficult to resolve. On the other hand, with longer length of the STF, i.e. larger number of basis functions, the fitted curve oscillates wildly and gives a very poor representation of the model, which is known as over-fitting. The length of the STF mentioned before was chosen to reach a compromise, after examining the residual misfit in total signal variance computed for different lengths of source time function. In order to

5 compensate travel-time residuals occurring along the mantle ray zero-lag Green functions are correlated with P-wave beams at every array, and the travel-time corrections are considered before the inversion. The source depth itself is estimated using a grid search approach, where the depth of the point source Green functions is sampled from 0 to 1000 m in 100 m steps. For every depth solution the residuals are estimated and stored for final evaluation.

Green functions are calculated using the code QSEIS (Wang, 1999), where source and station specific crustal models can be

10 considered. AK135 (Kennett et al., 1995) is used for the mantle, while different crustal models for source and station region are taken from (Bassin et al., 2000). Intrinsic attenuation for P-waves is set to 5000, since otherwise high frequencies are damped out at teleseismic distances. The sampling frequency is 20 Hz. The grid search depth phase modeling has been applied previously to different cases of induced seismicity (Dahm et al., 2007), but the simultaneous STF inversion is implemented for the first time.

15 The full waveforms of beams, their peak heights and peak distances are well fitted in a joint inversion of four arrays. The best fits are obtained at depths between 400 to 800 m (Figure 3b). However, it should be noted that the depth value obtained from the inversion procedure might be overestimated due to the use of an unperturbed velocity model. Perturbations in the velocity model for example through potential fracturing above the explosion, which would substantially reduced P-wave velocity, were neglected. If the source of the synthetic beams is placed deeper or shallower, the duration and appearance of the P-, pP- and

20 sP-pulses changes and residuals increase (compare Dahm et al., 2007). Interesting are the retrieved moment rate and moment function, which show a clear double pulse and overshoot, respectively (Figure 3c). Such an overshoot is not expected for the rupture process of tectonic earthquakes, but commonly observed for nuclear explosions. It can be explained by at least a partial collapse of the explosion cavity immediately after the explosion. In this case, the final moment is only 23 % of the peak moment in Figure 3c. The inversion of long-period waves led to a seismic moment M_0 of 2.33×10^{17} Nm, representing the

25 time after the overshoot. The peak seismic moment is thus estimated in the range of $M_{0,peak} \approx 1.02 \times 10^{18}$ Nm. The associated low and high frequency moment magnitudes (M_W) are $M_W=5.55$ and $M_W^{(peak)}=5.97$, respectively, and can explain the large difference between the long period M_W and the high-frequency m_b estimates in Subsection 2.4.

2.3 Moment Tensor Inversion of the Test and the Main Aftershock

Seismic signals of the 2017 North Korean test show a great similarity to those generated by the previous four nuclear tests

30 conducted in 2009, 2013, and 2016. Especially long period waveforms with periods above 10 s recorded at regional distances show a high waveform similarity and a substantially increased amplitude, revealing a very similar radiation pattern of all events and a larger moment release for the 2017 nuclear test. In recent years, MTIs have been performed for nuclear tests in North Korea, including those carried out in 2009, 2013 and 2016 (Ford et al., 2010; Barth, 2014; Vavryčuk and Kim, 2014; Cesca et al., 2017; Hartmann et al., 2017). All MTI were performed by fitting low-frequency full waveform seismic data at regional



distances, either in the time or in the frequency domain. The majority of these solutions revealed a significant positive isotropic component. For the 2013 nuclear test an extraordinary high double couple (DC) component was found, indicating differences in containment or near source damaging effects (Barth, 2014; Vavryčuk and Kim, 2014). For the 2017 test the seismic moment tensor is inverted by fitting the low frequency amplitude spectra (epicentral distances up to 1200 km) and full displacement waveforms (epicentral distances up to 600 km) in the frequency range from 0.02 to 0.04 Hz following the approach by Cesca et al. (2013, 2017). Full waveforms and their spectra are calculated assuming a layered crustal model proposed by Ford et al. (2010). Example full waveform displacement and amplitude spectra fits are shown in Figure 5.

Figure 5

10 The moment tensor solution for the 2017 test shows a dominant positive isotropic part of 60 %, 16 % positive compensated linear vector dipole (CLVD), and 24 % of DC. The best solution, found at a depth of around 2 km, has a scalar moment of 2.33×10^{17} Nm, equivalent to a M_W of 5.55. The moment tensor optimization resolves a broad ensemble of well fitting moment tensor solutions (Figure 6), either dominated by a positive isotropic component, a negative vertical CLVD, or a combination of both, what has been attributed to trade-offs among moment tensor components for very shallow sources (Cesca et al., 2017; Cesca and Heimann, 2017). This range of moment tensor solutions includes alternative moment tensor configurations as proposed for previous nuclear explosions in North Korea (e.g. Barth, 2014).

Figure 6

In the aftermath of the nuclear test, a seismic event took place in its direct vicinity around eight minutes later. The estimated scalar moment and M_W are 1.88×10^{16} Nm and 4.81, respectively, and thus the scalar moment is only ~ 8 % of the one of the nuclear test. The waveforms of the aftershock still show a good SNR, and the signal strength is sufficient to perform a MTI. Waveform displacement and amplitude spectra fits of the MTI are shown in Figure 7.

Figure 7

25 The inversion is based on spectral and waveform fits at stations located within 1000 km epicentral distance, filtered between 0.02 and 0.04 Hz. The calculated depth of the aftershock is similar to the depth of the explosion. The best MTI solution suggests a dominant implosive source component (65 %), negative CLVD (29 %) and a DC component of 6 %. This source mechanism is compatible with a shallow collapse source or might hint to some kind of break-in process. An ensemble of well fitting moment tensor solutions for this inversion is shown in Figure 8.

Figure 8

2.4 Magnitude and Yield Estimation

30 The determination of m_b is the prerequisite for a reliable estimation of the yield of a nuclear explosion. In order to obtain comparable results for the past six North Korean events, m_b is calculated from waveform peak values measured at always the



same 15 IMS seismic stations that recorded all six events. These stations cover the entire azimuthal range and are located at distances between 3700 and 9000 km from the Punggye-ri test site. For the 2017 test a m_b of 6.2 is calculated, compared to m_b values of 4.1 to 5.3 for the five preceding tests. In general it is not possible to state one single relation between magnitude and yield, as this relation depends on various factors, such as the geological setting at the source site, the efficiency of wave propagation from source to receiver, the depth of the explosion and the coupling of the source to the underground. A number of empirical formulas of the type $m_b = A + B \log(Y)$, with Y being seismic yield in kilotons TNT equivalent and A and B being constants depending on the aforementioned factors, have been developed to relate yield and m_b . These relations have been successfully used for yield calibration for example at the Nevada test site (Murphy, 1981), in Kazakhstan (Ringdal et al., 1992) or in Nova Zemlya (Bowers et al., 2001). As no particular magnitude-yield relation has been approved so far for the North Korean test area, the latter relation by Bowers et al. (2001) is used in this study, as it supposedly most accurately represents the geological conditions at the test site. Under these assumptions a yield of around 400 kilotons TNT equivalent is estimated for the September 2017 test, clearly illustrating a steady increase of explosive strength of the nuclear tests (see Figure 9).

Figure 9

2.5 Influence of the Mt. Mantap Topography

Two-dimensional synthetic wave-field simulations are used to study the influence of topography of the Mt. Mantap complex on the propagation of P- and S-wave energy emitted by a point-like explosion source. A Chebyshev pseudospectral method (e.g. Tessmer et al., 1992) is used for modeling the elastic wave-fields on a Cartesian 820×512 grid for an $8 \text{ km} \times 5 \text{ km}$ box in x- and z-direction, respectively. No variation of medium properties is assumed in the y-direction. Figure 10 shows the model configurations as well as the wave propagation for an explosion source in 0.8 km depth below surface (see Subsection 2.2).

Figure 10

The source time function is taken from Glasstone and Dolan (1977, Chapter 6), where the source duration is 0.15 s. The wave-field V is separated in divergence ($|\nabla \cdot V|$) and curl ($|\nabla \times V|$) reflecting the P- and SV-energy, respectively. Moreover, the wave propagation is considered for one model without and two models with topography; whereas the topography is considered for a west-east profile along 41.3°N crossing the Mt. Mantap massif (see Figure 1b). The velocity model is chosen such that it reflects the petrology of the local geology as described by Coblentz and Pabian (2015). However, strong lateral variations as thrust or normal faulting in the upper most layers are not taken into account due to reasons of numerical stability. Instead lateral variations, which are based on an exponential perturbation with a correlation length of 100 m, are considered with differences in density, P- and S-wave velocities of $\pm 3 \%$. Merely, the last model accounts for erosion of the upper most basaltic and volcanic layers as well as an almost vertical dyke reflecting the transition between the granodiorites and the granite from west to east. Nevertheless, computing the P-divergence and SV-curl in a rectangular box shows large differences in the downward propagating wave-fields, where strong increases for both pP- and pS-wave amplitudes can be observed. For a source under Mt. Mantap surface reflections are increased in their amplitudes by a factor of ~ 1.5 due to topography.

Wave energy is focused due to the shape of the mountain, especially from the easterly flank with a change in altitude of approx-



imately 600 m (see Figure 1b). Topography is the crucial factor, the difference between the two simulations with and without a realistic geologic setting (see Figure 10, middle and right panels) is negligible. Further simulations for sources shallower and deeper as the reference value of a depth of 0.8 km below surface provided similar pictures; whereas for sources shallower than 0.5 km and deeper than 1.7 km, respectively, is less pronounced with amplifications in amplitude of 1.3 and less. Although only a two-dimensional model is considered, such simulations are also valid for the three-dimensional nature because Mt. Mantap exhibits a high symmetry. In general, this numerical modeling gives indications for: (1) Clear infrasonic signals, because surface reflections with higher amplitudes correspond to transmitted amplitudes with higher amplitudes yielding a transmission coefficient greater than 2 (see Section 3). (2) A reduced value of the isotropic part obtained by MTI because a larger amount of S-wave energy is generated in the source region due to topography effects above the source (see Subsection 2.3). (3) An overestimation of the yield of the explosion, because P- and pP-phases are considered as a single onset in teleseismic distances and in the investigated frequency range for shallow sources, leading to an increase in maximum P-wave amplitude of approximately 1.3 and hence in m_b of around 0.1, respectively.

3 Infrasonic Observations

Infrasound is sub-audible sound below the human hearing threshold of 16 Hz and is the dedicated monitoring technology of the CTBTO for remotely detecting atmospheric explosions. Furthermore, infrasound can be used in civil and scientific applications such as the monitoring of volcanoes, meteoroids, ocean swell and various other natural and anthropogenic activities (see Le Pichon et al. (2010) for a comprehensive overview). Infrasound signals are also generated by strong underground or underwater sources when the generated waves couple into the atmosphere. The North Korean tests between 2006 and 2016 were investigated and registered by various infrasound arrays (Che et al., 2014; Assink et al., 2016; Park et al., 2018; Koch and Pilger, 2018). Detections of the 2013 test by the IMS stations I30JP in Japan and I45RU in Russia were part of the REB and thus confirmed the underground nuclear test as source of infrasound waves. For the 2017 test, the station I45RU detected infrasound signatures from the nuclear test site (see also Assink et al., 2018). Clear waveforms undoubtedly associated to the nuclear test were recorded and were again part of the REB. Figure 11a highlights the waveform beam of the Russian 4-element infrasound array I45RU (denoted as the co-located seismic station USRK in Figure 1a).

Figure 11

Coherent waveform signals can be observed and associated to infrasound propagation from the nuclear test site arriving at I45RU after travel times of 1450 s and 1520 s, corresponding to celerities of 290 m/s and 270 m/s, respectively. Preceding waveform activity at around 1350 s (315 m/s) can be associated to the fast acoustic phase of an infrasonic forerunner (Evers and Haak, 2007). These values are in the pure acoustic range and indicate stratospheric ducting (Is_2 with two reflections and Is_{1f} with one elongated reflection, turning heights of 40 to 55 km) and thermospheric ducting (It , turning heights above 100 km) (Drob et al., 2003). It is the first time that an underground nuclear test is strong enough to generate distinct and far-reaching pressure signatures that were clearly recorded at a remote IMS infrasound station after propagation through the thermosphere above 100 km altitude. The corresponding Progressive Multi-Channel Correlation (PMCC, Cansi, 1995) analysis



of the signal content in terms of time variation, frequency content and back-azimuth direction is illustrated in Figure 11b. The PMCC method draws rectangular time-frequency-windows wherever correlated signal energy in three or more array elements is present. Color-coded back azimuths between 210° and 225° (southwest) point towards the Punggye-ri nuclear test site with a true back-azimuth of 218° . Effects from cross winds (west to north-west, strongest in the stratosphere) lead to the fact that the observed back-azimuths are some degrees lower, especially within the stratospheric duct. The PMCC signatures with broadband frequency content from 0.2 to 4 Hz can thus clearly be associated to the 2017 DPRK nuclear test.

Figure 11c models the propagation from the test site epicenter to the station I45RU using parabolic equation and ray-tracing methods for the attenuation of signal amplitude and the connection of source and receiver by eigenrays. A combination of European Centre for Medium-Range Weather Forecasts (ECMWF) analysis data and climatological profiles is implemented for temperature and wind model backgrounds including gravity wave perturbations (see Koch and Pilger (2018) for further details on the methods and the atmospheric profiles used). The eigenrays show that the stratospheric phases are about 170 s and 70 s faster than the thermospheric phase (caused by a higher effective sound speed in the stratosphere and the longer wave path for the thermospheric phase). The signal attenuation indicates that only a small portion of signal energy is ducted in the stratosphere caused by partial reflections from gravity wave variations of the stratospheric mean background. This leads to higher attenuation in the stratospheric duct and thus stronger signal amplitudes in the thermospheric duct, which corresponds to the observed waveforms. The presented infrasound signals clearly observed even in 400 km distance and with disadvantageous propagation conditions are indicative for a strong surface movement in the epicentral area (see Section 4) of the underground test generating large acoustic pressure peaks as argued in Subsection 2.5. Apart from the strong epicentral surface movement, infrasonic signatures were also identified from seismo-acoustic coupling and the assumed cavity collapse associated to the eight minute subsequent aftershock.

4 Remote Sensing Studies

To visualize and characterize the surface imprint of the 2017 test radar data from the ALOS-2 satellite (Suzuki et al., 2009) and multispectral optical data from the Pleiades satellite (Gleyzes et al., 2012) are investigated. Data from the ALOS-2 satellite in the L-band (1257.5 MHz frequency, 3 m resolution) are analyzed by Interferometric synthetic aperture radar (InSAR) to investigate surface deformations (subsidence and uplift) correlated with the 2017 test and its aftershocks. The method of change detection analysis based on the Normalized Differential Vegetation Index (NDVI) is applied. Spaceborn InSAR has been used to detect surface displacements of the Earth's surface since more than 20 years (Massonnet et al., 1993) and has reached maturity in recent years (Adam et al., 2009), nowadays allowing for the detection of surface displacements with a precision in the order of a few millimeters. Repeat pass interferometry is based on the registered interferometric phase per ground cell (pixel) and is related to the distance differences between the scatterer and the SAR sensor between two acquisitions separated in time. The interferometric phase measured as moduli 2π is thus ambiguous. To solve this ambiguity, frequency estimations using unwrapping techniques are calculated. The Earth's curvature, topography and atmospheric effects influence the interferometric phase in addition to surface displacements. These phase contributions have to be estimated and subtracted to



correctly estimate the surface displacement (Kampes, 2006). In addition, the backscattered electromagnetic signal between the acquisitions times needs to be correlated or coherent. Decorrelation can be caused by (1) temporal (large separation between the acquisitions in time), (2) geometrical (large perpendicular baseline) and (3) scattering effects (incoherent movement of scattering elements within the pixel, Gatelli et al., 1994).

5 Differential InSAR (DInSAR) processing was adjusted to the test site target area regarding above mentioned constraints. As the investigated area is located in a mountainous region, DInSAR processing is challenging due to factors such as limited visibility for SAR acquisition geometry, tropospheric phase contributions and/or snow cover and vegetation causing temporal phase decorrelations. DInSAR processing encompasses following steps: co-registration, filtering, unwrapping and the discussion of coherence. Coherence serves as a measure of the quality in DInSAR studies, with coherence values ranging from 0.0 to 1.0, with
10 1.0 suggesting a perfect interferogram with no noise. For the analysis of the surface displacement due to the 2017 test, data from August 29th and from September 12th 2017 is used, data coherence between these two times has a mean value of 0.6 for the investigated area. For areas that show surface deformation the coherence values range from 0.2 to 0.8.

Figure 12 shows the surface deformation restricted to the test site area after the 2017 test for pixels with a coherence of greater than 0.25.

15

Figure 12

In the central part of the Mt. Mantap massive, coherence values dropped significantly below 0.25 due to very strong ground deformations (see also Wang et al., 2018) The recognition of the displacements is only possible in line of sight in the direction towards or away from the sensor. Due to the incidence (43°) and look angle (ENE) of the sensors and the calculated slope and aspect angle (20 to 27° facing SW, 10° facing NE) based on Shuttle Radar Topography Mission data, 30 to 80 % of the vertical
20 measured displacements in the area are detected. The resulting displacement map clearly shows an area of subsidence of up to 10 cm around 3 km north of the tunnel entrance (compare Figure 1b), and an area with clear uplift of up to 10 cm west of the Mt. Mantap peak. DInSAR processing of C-Band Sentinel data and TerraSAR-X data for the 2017 test did not reveal acceptable quality measures regarding coherence in the central part of Mt. Matap, whereas for the tests in 2016 Sentinel data did show excellent results (Hartmann et al., 2017; Wei, 2017). A study by Wang et al. (2018) shows additional results based on
25 amplitude images from TerraSAR-X data and calculates 0.5 m subsidence in the centre and 3.5 m of horizontal displacement. This strong spatial and temporal coincidence of the displacement areas to the nuclear test site suggests a high correlation with the underground test.

To validate the displacement maps of the DInSAR analysis of the nuclear test, Pleiades data sets from August 26th and from September 8th 2017 were processed to reveal surface characteristics related to test (Figure 13).

30

Figure 13

Change detection analysis show numerous landslides activated during the test and aftershocks. As a result of the processing of the ALOS-2 data, an area of around $3 \times 4 \text{ km}^2$ can be delineated, where surface movement rates range between -10 and 10 cm.



5 Radionuclide Monitoring and Atmospheric Transport Modeling

Measurements of radioactive fission products released into the atmosphere even at far distances can deliver the definite proof of the nuclear character of an explosion. To assess the consistency between measurements and potential source locations the method of ATM is applied (Becker et al., 2007; Ross et al., 2017). For the ATM analysis of potential detections of radionuclides the Lagrangian Particle Dispersion Model HYSPLIT (National Oceanic and Atmospheric Administration – Air Resources Laboratory, Stein et al., 2015) is used. The ATM is operated with meteorological data from the US National Centers for Environmental Prediction (NCEP). For the prediction of potentially affected radionuclide measurement stations, HYSPLIT is operated in forward mode with hypothetical releases. For the assessment of the potential source region of detected radioisotopes the model runs in backward mode. Dispersion simulations of a potential immediate release after the explosion on September 3rd 2017 show prevailing wind directions to the north east (Figure 14a).

Figure 14

The IMS station RN58 (Ussuryysk, Russia) would have been affected, but was not operational at that time. Station RN38 (Takasaki, Japan) would have been missed by the plume from the potential release from the test site which is typical for the season. Stations further downwind, for example in Northern America, would have required a larger release for activity concentrations to exceed the detection threshold.

The South Korean Nuclear Safety and Security Commission issued a press release on September 13th 2017 with results of national efforts to detect radioactive Xe isotopes after the test. The statement '*Considering the timing and location of sampling and air currents, the NSSC could conclude that the air currents from the North Punggye-ri area has been mixed to the sample and the Xe-133 detected from this air sampling is relevant to the 6th nuclear test of DPRK*' (Nuclear Safety and Security Commission, 2017) was interpreted by the media as source attribution. Backward simulations for the samples collected at the northeastern stationary measurement system at Geojin were performed using 500000 model particles per sample and 0.5° GDAS (Global Data Assimilation System) meteorological data. Additive overlay of the source regions of seven stationary 12-hour samples with elevated ^{133}Xe from September 7th to 10th 2017 points to the Nyongbyon County, and area where the North Korean Scientific Research Center is located, as likely coincident source (Figure 14b), whereas the test site can be disregarded as common source for the seven samples. This contradicts the suggestions in the media that the detected ^{133}Xe originated from the test explosion.

Forward simulations from the test site show that the station RN58 would have been affected by hypothetical releases in October repeatedly. Figure 14c shows the dispersion after 36 h of a hypothetical ten hour release on October 4th 2017 using HYSPLIT with 0.25° GFS (Global Forecast System) data and 1 million particles released. During October three peaks containing five samples with ^{133}Xe activity concentrations between 0.5 and 1 mBq/m³ were measured at the station RN58, which went back to operation in between, at the days indicated by the forward simulations.

Backward ATM results also indicate a high sensitivity of these five samples to being released from the test site. Figure 14d shows the overlap of the corresponding retroplumes at time of maximum sensitivity to the test site. A leakage in the order of 10¹¹ Bq ^{133}Xe would have been sufficient to explain the detections at station RN58. Although the measurements and the ATM



are consistent with delayed small releases from the test site in October, they cannot be unambiguously attributed to the North Korean test explosion.

6 Discussion

Seismological analysis using a double-difference method result in an epicenter location of the 2017 test of 41.3007°N, 129.0728°E, clearly placing the event inside the North Korean nuclear test site, in which all previous tests have been conducted. The epicenter location is confirmed by results from (Wang et al., 2018), who estimated an epicenter location of 41.300°N, 129.078°E \pm 50 m, which places the two epicenter solutions only \sim 400 to 500 m apart. On May 24th 2018 North Korea invited international media to witness the demolition of the Punggye-ri test site. During a demonstration North Korean officials presented a map showing the relative locations of the six nuclear tests (CNN, 2018). Although the correctness of the information provided by the North Korean government cannot be verified, comparisons indicate that the assumed locations fit the results from the independent relative location method reasonably well. Two independent methods showed that the 2017 North Korea event was very shallow. The full waveform moment tensor inversion indicates a centroid depth in the range of about 2 km, but has a relatively poor resolution because of the long wavelength of lowpass filtered data. The depth phase modeling of the P-waveform was performed at 2.5 Hz and found a centroid depth between 400 m and 800 m, which is within the expected resolution of about half the wavelength. This is supposedly the best absolute centroid depth estimate possible from seismological data far from the source. Depth estimations in this study are comparable to results from Wang et al. (2018). The authors used numerical models to minimize the misfit between predicted and observed surface displacements and specified a depth of 450 \pm 100 m.

The explosive character of the 2017 event is confirmed by MTI analysis, which indicates a dominant isotropic source part of around 60 %. These results are supported by studies by Liu et al. (2018) and Han et al. (2017), who also revealed a dominant positive isotropic source part. Under the assumption of the magnitude-yield relation following Bowers et al. (2001) the estimated m_b of 6.2 (see Subsection 2.4) for the event results in a yield of 400 kilotons TNT equivalent. This value is assumed to be an upper limit, as following reasons might lead to a yield overestimation: (1) Topography at the test site (see Subsection 2.5) strongly influences the radiation of seismic energy from the source. This results in higher amplitudes of the pP-phase. As the hypocenter location is very shallow, P- and pP-phases from the event arrive nearly simultaneously at distant receivers and superimpose at frequencies relevant for the estimation of m_b . This superimposition leads to an increase of approximately 1.3 in P-wave amplitude in the far-field and consequently to an increase in m_b of around 0.1. (2) Furthermore in the standard calculations of m_b (Gutenberg, 1945a, b; Bormann, 2012), distant-dependent correction curves, which are valid for a DC source, are applied. Gaebler and Ceranna (2017) state, that the use of correction terms for a shallow explosion source can lead to an overestimation of m_b of around 0.2. Taking both these effects into account, the originally estimated value for m_B of 6.2 had to be considered as an upper limit estimate and has to be corrected by a factor of up to 0.3. This correction leads to a lower estimate for m_B of 5.9, similar to $M_W^{(\text{peak})}$ that is estimated from the source time function, which translates to an estimated yield of around 160 kilotons TNT equivalent. Therefore indications are strong that yield might be overestimated, not only for



the 2017 explosion, but also for all five previous North Korean nuclear tests.

Following the main event around eight minutes later a large aftershock of local magnitude m_L 4.1 was detected. MTI analysis of this event shows a clear negative isotropic part which leads to the conclusion that this event is at least a partial collapse of the cavity formed by the main explosion. This findings are again supported Liu et al. (2018) and Han et al. (2017), who also
5 find a clear negative isotropic source part for the aftershock. According to Liu et al. (2018), the aftershock can qualitatively be interpreted as a rapid destruction of an explosion-generated cracked rock chimney due to cavity collapse. Following this strong aftershock, nine more earthquakes with local magnitudes m_L ranging from 2.5 up to 3.2 were detected by the Korean Meteorological Agency (Korean Meteorological Agency, 2018) in the region (41.2 to 41.4°N, 129.0 to 129.2°E) until April 2018. Aftershocks in such magnitude range and quantity were not observed from the five previous tests from 2006 to 2016, but are
10 not unusual for nuclear explosions of that size (Boucher et al., 1969).

In the aftermath of the 2017 event measurable surface activity was detected in the region of the Punggye-ri test site. Remote sensing results suggest a distinct pattern of uplift (up to 10 cm) in the western part of the Mt. Mantap massif and subsidence (up to -10 cm) in the eastern part. The geological interpretation by Coblenz and Pabian (2015) and Pabian and Coblenz (2017) shows a north-south trend of various geological units ranging from carbonates, diorites, granites and gneisses in contact
15 to a younger basalt (layered volcanics) at Mt. Mantap. Furthermore, the structural pattern in the region suggests a north-south trending system of faults up to the main tunnel entrances, with a part of the fault system branching out to the north-west. Considering this geological background the deformation pattern can be interpreted as a (partial) uplift of the basement rocks in the western part. Eventually this is structurally controlled by the north-south trending reverse faults together with the unconformable capping of stratified volcanic sequences. This interpretation is confirmed by multispectral optical data from the
20 Pleiades satellite which shows that the layered tuffs are strongly affected by intensive landslide activities.

Overall, accounting for all these activities (surface deformations, the collapse event, aftershocks, landslides) it can be argued, that the internal structure beneath Mt. Mantap might be strongly stressed and shattered due to the last six tests and might be rendered useless for further test explosions (see also Wang et al., 2018).

Despite these strong activities and the enormous release of seismic energy from the event no immediate release of radionuclides
25 was measured by the IMS. This is a strong indication that no direct pathways from the cavity to the surface for the propagation of radionuclides were created during the test and the subsequent collapse-type aftershock. Only a few days after the 2017 event South Korea announced national measurements of ^{133}Xe and proposed a connection of these observations to the test. However, backward ATM calculations performed in the context of this study disfavor the Punggye-ri test site as possible origin for ^{133}Xe but rather point to the Yongbyon nuclear complex as a most likely coincident source region instead in September. Nevertheless,
30 in October 2017 three peaks of ^{133}Xe were detected at the IMS station RN58 in Ussurysk, Russia. Forward as well as backward ATM show directly connecting dispersion conditions and indicate the North Korean test site as a likely source for the ^{133}Xe detections. Nevertheless, other regional sources cannot be excluded and it was not possible to definitely identify the presence of ^{131m}Xe in the RN58 samples, which – in the correct isotropic ratio – would have increased the evidence of a nuclear explosion source (Kalinowski et al., 2010), as for example shown for the 2013 North Korean nuclear explosion by Ringbom et al. (2014).
35 According to calculations of concentration and sensitivity, a release at the test site in the order of a few 10^{11} Bq would have



been sufficient to cause and explain the detections at station RN58. This is also quantitatively consistent as the required source term ranges well below the remaining fission inventory even after six to ten half-lives of ^{133}Xe (5.2 days) and a small leakage through mountain cracks. However, a direct number of the fission inventory is hard to estimate as the fission yield depends not only on the explosive yield but also on the type of nuclear device. Within the available data it is not possible to determine

5 if nuclear fusion was involved in the process. The largest yield ever achieved by a boosted fission device was 720 kT TNT equivalent of the British *Orange Herald* in 1957. For this explosion an amount of 118 kg ^{235}U was mounted (Arnold and Pyne, 2001). The explosive yield in this study of between 160 and 400 kT TNT equivalent is therefore still fully compatible with a fission only device.

DInSAR results show a large area of strong displacement in the case of the 2017 test and it is not possible to demarcate a definite

10 surface location of the test epicenter from these measurements. However retrieving a ground truth from DInSAR measurements from the January 2016 test, which showed a clear and distinct maximum of surface displacement, can help to provide an absolute epicenter location of the 2017 test. By combining remote sensing and relative locations methods only the epicenter of the event can be estimated. A third method (depth phase modeling) is required for the complete estimation of the 2017 test hypocenter. This method is further able to provide an explanation for the large difference in m_b and M_W , which has not been

15 observed in this order for the previous tests. Furthermore while for previous weaker tests radionuclide measurements were able to prove the nuclear character of the explosions (Ross et al., 2017), radionuclide measurements alone in September 2017 could have been misleading in regards to the source area. This examples clearly demonstrate that an integrated multi-technology and multi-methodology approach is essential for a reliable and comprehensive identification and characterization of a potential nuclear test.

20 7 Conclusions

Overall, the following main conclusions can be deduced from this study:

- Explosive character of the September 3rd 2017 North Korean event is confirmed by cross correlation and MTI analysis.
- Yield of the event is estimated to be around 400 kt TNT equivalent with indications that this value should be considered as an upper limit and might be as low as 160 kt TNT equivalent. This overestimation can be explained by the enhancement
- 25 of peak amplitudes of teleseismic P-waves due to topography and depth phase effects.
- The estimated yield of the nuclear device is certainly smaller than the largest documented yield ever achieved by a boosted fission device and is therefore still compatible with a fission only device.
- Strong surface deformations (± 10 cm) are observed in an area of 3×4 km². Furthermore multiple landslides as well as a number of aftershocks were observed in the aftermath of the test.
- 30 • The aftershock directly following the nuclear explosion has a similar depth as the test and can be characterized as a collapse of the cavity created by the test.



- Infrasound signals measured at the station I45RU can clearly be related to the 2017 event. It is the first time that a thermospheric propagation path of infrasound could be observed for an underground nuclear explosion.
 - No immediate measurements of radionuclides related to the test in September were observable, but later occurrences of radionuclides are consistent with a delayed leakage from the test site in October.
- 5 • The test site might be strongly stressed and shattered and might be rendered useless for further test activities.

The multi-technology and multi-methodology analysis presented in this study, clearly indicates that the September 2017 North Korean event was in fact a nuclear test. Even in the phase of pre entry-into-force the CTBTO verification regime has again demonstrated its readiness with respect to the recent nuclear test.

Data. The facilities of IRIS Data Services, and specifically the IRIS Data Management Center, were used for access to seismic waveforms, related metadata, and/or derived products used in this study. IRIS Data Services are funded through the Seismological Facilities for the Advancement of Geoscience and EarthScope (SAGE) Proposal of the National Science Foundation under Cooperative Agreement EAR-1261681. Seismic, infrasound and radionuclide data from stations of the IMS network (seismic, infrasound, radionuclide) were obtained by the German NDC through the IDC of the CTBTO. ECMWF operational analysis data is used for infrasound propagation modeling. ATM using HYSPLIT is operated with GDAS and GFS meteorological data from the United States NCEP. Satellite from ALOS-2 was obtained by GAF AG, data from the Pleiades satellite was delivered by Airbus Defence and Space.

Acknowledgements. The critical and helpful comments by Stefanie Donner (BGR) and Patrick Hupe (BGR) are highly appreciated. Furthermore we highly appreciate comments by Michael Ritzwoller (CU) and Jörg Renner (RUB) as well as by two anonymous reviewers. NN acknowledges support from the German Federal Ministry of Education and Research in the context of the project SECURE (FKZ-03A0013A).

Author contributions. Authors contributions to the different Sections and Subsections of this study, including data analysis and interpretation, preparation of the figures and results, as well as writing, is as following: Subsection 2.1 Epicenter location: GH and PG. Subsection 2.2 Estimation of Hypocenter Depth and Seismic Moment: SC, TD, NN. Subsection 2.3 Moment Tensor Inversion of the Test and the Main Aftershock: AB, SC, and TD. Subsection 2.4 Magnitude and Yield Estimation: GH and PG. Subsection 2.5 Influence of the Mt. Mantap Topography: LC and PG. Section 3 Infrasound Observations: CP, KK, LC and PG. Section 4 Remote Sensing Studies: MF and IG. Section 5 Radionuclide Monitoring and Atmospheric Transport Modeling: OR and PG. PG, LC and TD devised and finalized the original manuscript.

Competing interests. The authors declare that they have no conflict of interest.



References

- Adam, N., Parizzi, A., Eineder, M., and Crosetto, M.: Practical persistent scatterer processing validation in the course of the TerraFirma project, *Journal of Applied Geophysics*, 69, 59 – 65, <https://doi.org/https://doi.org/10.1016/j.jappgeo.2009.07.002>, advances in SAR Interferometry from the 2007 Fringe Workshop, 2009.
- 5 Arnold, L. and Pyne, K.: The First Trial — Grapple, pp. 131–150, Palgrave Macmillan UK, London, https://doi.org/10.1057/9780230599772_10, 2001.
- Assink, J., Averbuch, G., Shani-Kadmiel, S., Smets, P., and Evers, L.: A Seismo-Acoustic Analysis of the 2017 North Korean Nuclear Test, *Seismological Research Letters*, <https://doi.org/10.1785/0220180137>, 2018.
- Assink, J. D., Averbuch, G., Smets, P. S. M., and Evers, L. G.: On the infrasound detected from the 2013 and 2016 DPRK's underground
10 nuclear tests, *Geophysical Research Letters*, 43, 3526–3533, <https://doi.org/10.1002/2016GL068497>, 2016.
- Barth, A.: Significant release of shear energy of the North Korean nuclear test on February 12, 2013, *Journal of Seismology*, 18, 2014.
- Bassin, C., Laske, G., and Masters, G.: The Current Limits of Resolution for Surface Wave Tomography in North America, *Eos*, 81, 2000.
- Becker, A., Wotawa, G., De Geer, L.-E., Seibert, P., Draxler, R. R., Sloan, C., D'Amours, R., Hort, M., Glaab, H., Heinrich, P., Grillon, Y.,
15 Shershakov, V., Katayama, K., Zhang, Y., Stewart, P., Hirtl, M., Jean, M., and Chen, P.: Global backtracking of anthropogenic radionuclides
by means of a receptor oriented ensemble dispersion modelling system in support of Nuclear-Test-Ban Treaty verification, *Atmospheric
Environment*, 41, 4520–4534, <https://doi.org/https://doi.org/10.1016/j.atmosenv.2006.12.048>, 2007.
- Bormann, P.: New Manual of Seismological Observatory Practice (NMSOP-2), Deutsches GeoForschungszentrum GFZ ; IASPEI, Potsdam,
<https://doi.org/10.2312/GFZ.NMSOP-2>, 2012.
- Boucher, G., Ryall, A., and Jones, A. E.: Earthquakes associated with underground nuclear explosions, *Journal of Geophysical Research*, 74,
20 3808–3820, <https://doi.org/10.1029/JB074i015p03808>, 1969.
- Bowers, D., Marshall, P. D., and Douglas, A.: The level of deterrence provided by data from the SPITS seismometer array to possible violations of the Comprehensive Test Ban in the Novaya Zemlya region, *Geophysical Journal International*, 146, 425–438,
<https://doi.org/10.1046/j.1365-246x.2001.01462.x>, 2001.
- Cansi, Y.: An automatic seismic event processing for detection and location: The P.M.C.C. Method, *Geophysical Research Letters*, 22,
25 1021–1024, <https://doi.org/10.1029/95GL00468>, 1995.
- Cesca, S. and Heimann, S.: Moment Tensor Solutions - A Useful Tool for Seismotectonics, chap. Challenges in regional moment tensor resolution and interpretation, Springer Natural Hazards, <https://doi.org/10.1007/978-3-319-77358-2>, 2017.
- Cesca, S., Rohr, A., and Dahm, T.: Discrimination of induced seismicity by full moment tensor inversion and decomposition, *Journal of Seismology*, 17, 147–163, 2013.
- 30 Cesca, S., Heimann, S., Kriegerowski, M., Saul, J., and Dahm, T.: Moment Tensor Inversion for Nuclear Explosions: What Can We Learn from the 6 January and 9 September 2016 Nuclear Tests, North Korea?, *Seismological Research Letters*, 88, 300,
<https://doi.org/10.1785/0220160139>, 2017.
- Che, I.-Y., Park, J., Kim, I., Kim, T. S., and Lee, H.-I.: Infrasound signals from the underground nuclear explosions of North Korea, *Geophysical Journal International*, 198, 495–503, <https://doi.org/10.1093/gji/ggu150>, 2014.
- 35 CNN: North Korea blows up tunnels at Punggye-ri nuclear test site, <https://edition.cnn.com/2018/05/24/asia/north-korea-nuclear-test-site-intl/index.html>, 2018.



- Coblentz, D. and Pabian, F.: Revised Geologic Site Characterization of the North Korean Test Site at Punggye-ri, *Science & Global Security*, 23, 101–120, 2015.
- CTBTO: Preparatory Commission for the Comprehensive Nuclear-Test-Ban Treaty Organization, <https://www.ctbto.org/>, 2018.
- Dahm, T. and Krüger, F.: New Manual of Seismological Observatory Practice (NMSOP-2), IASPEI, GFZ German Research Centre for Geosciences, Potsdam; <http://nmsop.gfz-potsdam.de>, chap. Moment tensor inversion and moment tensor interpretation, Deutsches Geoforschungszentrum GFZ, Potsdam, Germany, https://doi.org/10.2312/GFZ.NMSOP-2_IS_3.9, 2014.
- Dahm, T., Küger, F., Stammer, K., Klinge, K., Kind, R., Wylegalla, K., and Grasso, J.-R.: The 2004 Mw 4.4 Rotenburg, Northern Germany, Earthquake and Its Possible Relationship with Gas Recovery, *Bulletin of the Seismological Society of America*, 97, 691, <https://doi.org/10.1785/0120050149>, 2007.
- Drob, D. P., Picone, J. M., and Garcés, M.: Global morphology of infrasound propagation, *Journal of Geophysical Research*, 108, 13–1–13–12, <https://doi.org/10.1029/2002JD003307>, 4680, 2003.
- Evers, L. G. and Haak, H. W.: Infrasonic forerunners: Exceptionally fast acoustic phases, *Geophysical Research Letters*, 34, <https://doi.org/10.1029/2007GL029353>, 110806, 2007.
- Ford, S. R., Dreger, D. S., and Walter, W. R.: Network Sensitivity Solutions for Regional Moment-Tensor Inversions, *Bulletin of the Seismological Society of America*, 100, 1962, <https://doi.org/10.1785/0120090140>, 2010.
- Gaebler, P. J. and Ceranna, L.: Monitoring Compliance with the Comprehensive Nuclear-Test-Ban Treaty (CTBT). Contributions by the German National Data Center, chap. The Seismic Network of the International Monitoring System (IMS), pp. 69–90, Schweizerbart Science Publishers, Stuttgart, Germany, 2017.
- Gatelli, F., Monti Guamieri, A., Parizzi, F., Pasquali, P., Prati, C., and Rocca, F.: The Wavenumber Shift in SAR Interferometry, 29, 855 – 865, 1994.
- Gibbons, S. J., Pabian, F., Näsholm, S. P., Kväerna, T., and Mykkeltveit, S.: Accurate relative location estimates for the North Korean nuclear tests using empirical slowness corrections, *Geophysical Journal International*, 208, 101–117, <https://doi.org/10.1093/gji/ggw379>, 2017.
- Glasstone, S. and Dolan, P. J.: *The Effects of Nuclear Weapons*, U.S. Government Printing Office, 1977.
- Gleyzes, M. A., Perret, L., and Kubik, P.: Pleiades System Architecture and Main Performances, *ISPRS - International Archives of the Photogrammetry, Remote Sensing and Spatial Information Sciences*, pp. 537–542, <https://doi.org/10.5194/isprsarchives-XXXIX-B1-537-2012>, 2012.
- Gutenberg, B.: Amplitudes of P, PP, and S and magnitude of shallow earthquakes*, *Bulletin of the Seismological Society of America*, 35, 57, 1945a.
- Gutenberg, B.: Magnitude determination for deep-focus earthquakes*, *Bulletin of the Seismological Society of America*, 35, 117, 1945b.
- Han, L., Wu, Z., Jiang, C., and Liu, J.: Properties of three seismic events in September 2017 in the northern Korean Peninsula from moment tensor inversion, *Science Bulletin*, 62, 1569 – 1571, <https://doi.org/https://doi.org/10.1016/j.scib.2017.11.007>, 2017.
- Hartmann, G., Barth, A., Ross, J. O., Grünberg, I., and Frei, M.: Monitoring Compliance with the Comprehensive Nuclear-Test-Ban Treaty (CTBT). Contributions by the German National Data Center, chap. Verification of the North Korean Nuclear Explosions 2006, 2009, 2013, and 2016, pp. 137–165, Schweizerbart Science Publishers, Stuttgart, Germany, 2017.
- Hudson, J. A., Pearce, R. G., and Rogers, R. M.: Source type plot for inversion of the moment tensor, *Journal of Geophysical Research: Solid Earth*, 94, 765–774, <https://doi.org/10.1029/JB094iB01p00765>, 1989.



- Kalinowski, M., Axelsson, A., Bean, M., Blanchard, X., Bowyer, T., Brachet, G., Hebel, S., McIntyre, J., Peters, J., Pistner, C., Raith, M., Ringbom, A., R. J. Saey, P., Schlosser, C., J. Stocki, T., Taffary, T., and Ungar, K.: Discrimination of Nuclear Explosions against Civilian Sources Based on Atmospheric Xenon Isotopic Activity Ratios, *Pure and Applied Geophysics*, 167, 517–539, 2010.
- Kampes, B. M.: Radar Interferometry – Persistent Scatterer Technique, Springer Netherlands, <https://doi.org/10.1007/978-1-4020-4723-7>,
5 2006.
- Kennett, B. L. N., Engdahl, E. R., and Buland, R.: Constraints on seismic velocities in the Earth from traveltimes, *Geophysical Journal International*, 122, 108–124, <https://doi.org/10.1111/j.1365-246X.1995.tb03540.x>, 1995.
- Koch, K. and Pilger, C.: Infrasound observations from the site of past underground nuclear explosions in North Korea, *Geophysical Journal International*, p. ggy381, <https://doi.org/10.1093/gji/ggy381>, 2018.
- 10 Korean Meteorological Agency: http://www.weather.go.kr/weather/earthquake_volcano/domesticlist.jsp?startTm=2017-09-01&endTm=2018-12-13&startSize=999&endSize=999&startLat=41.2&endLat=41.4&startLon=129&endLon=129.2&lat=&lon=&dist=&keyword=&x=36&y=11, 2018.
- Le Pichon, A., Blanc, E., and Hauchecorne, A.: Infrasound Monitoring for Atmospheric Studies, Springer, <https://doi.org/10.1007/978-1-4020-9508-5>, 2010.
- 15 Liu, J., Li, L., Zahradník, J., Sokos, E., Liu, C., and Tian, X.: North Korea's 2017 Test and its Nontectonic Aftershock, *Geophysical Research Letters*, 45, 3017–3025, <https://doi.org/10.1002/2018GL077095>, 2018.
- Massonnet, D., Rossi, M., Carmona, C., Adragna, F., Peltzer, G., Feigl, K., and Rabaute, T.: The displacement field of the Landers earthquake mapped by radar interferometry, *Nature*, 364, 138–142, <https://doi.org/doi:10.1038/364138a0>, 1993.
- Murphy, J. R.: Identification of Seismic Sources — Earthquake or Underground Explosion, chap. P Wave Coupling of Underground Explosions in Various Geologic Media, pp. 1201–205, Springer Netherlands, Dordrecht, <https://doi.org/10.1007/978-94-009-8531-5>, 1981.
- 20 Nuclear Safety and Security Commission: Press Release: Radionuclide Detection After the 6th North Korea Nuclear Test, http://www.nssc.go.kr/_custom/nssc/_common/board/download.jsp?attach_no=20247, 2017.
- Pabian, F. and Coblentz, D.: Surface Disturbances at the Punggye-ri Nuclear Test Site: Another Indicator of Nuclear Testings?, Los Alamos National Laboratory. Report posted on 38north.org, final version issued March 15, 2017, 2017.
- 25 Park, J., Che, I.-Y., Stump, B., Hayward, C., Dannemann, F., Jeong, S., Kwong, K., McComas, S., Oldham, H. R., Scales, M. M., and Wright, V.: Characteristics of infrasound signals from North Korean underground nuclear explosions on 2016 January 6 and September 9, *Geophysical Journal International*, 214, 1865–1885, 2018.
- Pilger, C., Ceranna, L., and Bönnemann, C.: Monitoring Compliance with the Comprehensive Nuclear-Test-Ban Treaty (CTBT). Contributions by the German National Data Center, Schweizerbart Science Publishers, Stuttgart, Germany, 2017.
- 30 Ringbom, A., Axelsson, A., Aldener, M., Auer, M., Bowyer, T., Fritioff, T., Hoffman, I., Khrustalev, K., Nikkinen, M., Popov, V., Popov, Y., Ungar, K., and Wotawa, G.: Radioxenon detections in the CTBT international monitoring system likely related to the announced nuclear test in North Korea on February 12, 2013, *Journal of Environmental Radioactivity*, 128, 47 – 63, <https://doi.org/https://doi.org/10.1016/j.jenvrad.2013.10.027>, 2014.
- Ringdal, F., Marshall, P. D., and Alewine, R. W.: Seismic yield determination of Soviet underground nuclear explosions at the Shagan River test site, *Geophysical Journal International*, 109, 65–77, <https://doi.org/10.1111/j.1365-246X.1992.tb00079.x>, 1992.
- 35 Ross, J. O., Bollhöfer, A., and Schlosser, C.: Monitoring Compliance with the Comprehensive Nuclear-Test-Ban Treaty (CTBT). Contributions by the German National Data Center, chap. The IMS Radionuclide Network Supported by Atmospheric Transport Modelling (ATM), pp. 123–136, Schweizerbart Science Publishers, Stuttgart, Germany, 2017.



- Stein, A. F., Draxler, R. R., Rolph, G. D., Stunder, B. J. B., Cohen, M. D., and Ngan, F.: NOAA's HYSPLIT Atmospheric Transport and Dispersion Modeling System, *Bulletin of the American Meteorological Society*, 96, 2059–2077, <https://doi.org/10.1175/BAMS-D-14-00110.1>, 2015.
- Suzuki, S., Osawa, Y., Hatoooka, Y., Kankaku, Y., and Watanabe, T.: Overview of Japan's Advanced Land Observing Satellite-2 mission, <https://doi.org/10.1117/12.831340>, 2009.
- 5 Tessmer, E., Kosloff, D., and Behle, A.: Elastic wave propagation simulation in the presence of surface topography, *Geophysical Journal International*, 108, 621–632, <https://doi.org/10.1111/j.1365-246X.1992.tb04641.x>, 1992.
- Vavryčuk, V. and Kim, S. G.: Nonisotropic radiation of the 2013 North Korean nuclear explosion, *Geophysical Research Letters*, 41, 7048–7056, <https://doi.org/10.1002/2014GL061265>, 2014.
- 10 Waldhauser, F. and Ellsworth, W. L.: A Double-Difference Earthquake Location Algorithm: Method and Application to the Northern Hayward Fault, California, *Bulletin of the Seismological Society of America*, 90, 1353–1368, <https://doi.org/10.1785/0120000006>, 2000.
- Wang, R.: A simple orthonormalization method for stable and efficient computation of Green's functions, *Bulletin of the Seismological Society of America*, 89, 733, 1999.
- Wang, T., Shi, Q., Nikkhoo, M., Wei, S., Barbot, S., Dreger, D., Bürgmann, R., Motagh, M., and Chen, Q.-F.: The rise, collapse, and compaction of Mt. Mantap from the 3 September 2017 North Korean nuclear test, *Science*, <https://doi.org/10.1126/science.aar7230>, 2018.
- 15 Wei, M.: Location and source characteristics of the 2016 January 6 North Korean nuclear test constrained by InSAR, *Geophysical Journal International*, 209, 762–769, <https://doi.org/10.1093/gji/ggx053>, 2017.
- Zhang, M. and Wen, L.: High-precision location and yield of North Korea's 2013 nuclear test, *Geophysical Research Letters*, 40, 2941–2946, <https://doi.org/10.1002/grl.50607>, 2013.
- 20 Zhao, L., Xie, X., Wang, W., and Yao, Z.: The 12 February 2013 North Korean Underground Nuclear Test, *Seismological Research Letters*, 85, 130–134, <https://doi.org/10.1785/0220130103>, 2014.
- Zhao, L.-F., Xie, X.-B., Wang, W.-M., Hao, J.-L., and Yao, Z.-X.: Seismological investigation of the 2016 January 6 North Korean underground nuclear test, *Geophysical Journal International*, 206, 1487–1491, <https://doi.org/10.1093/gji/ggw239>, 2016.

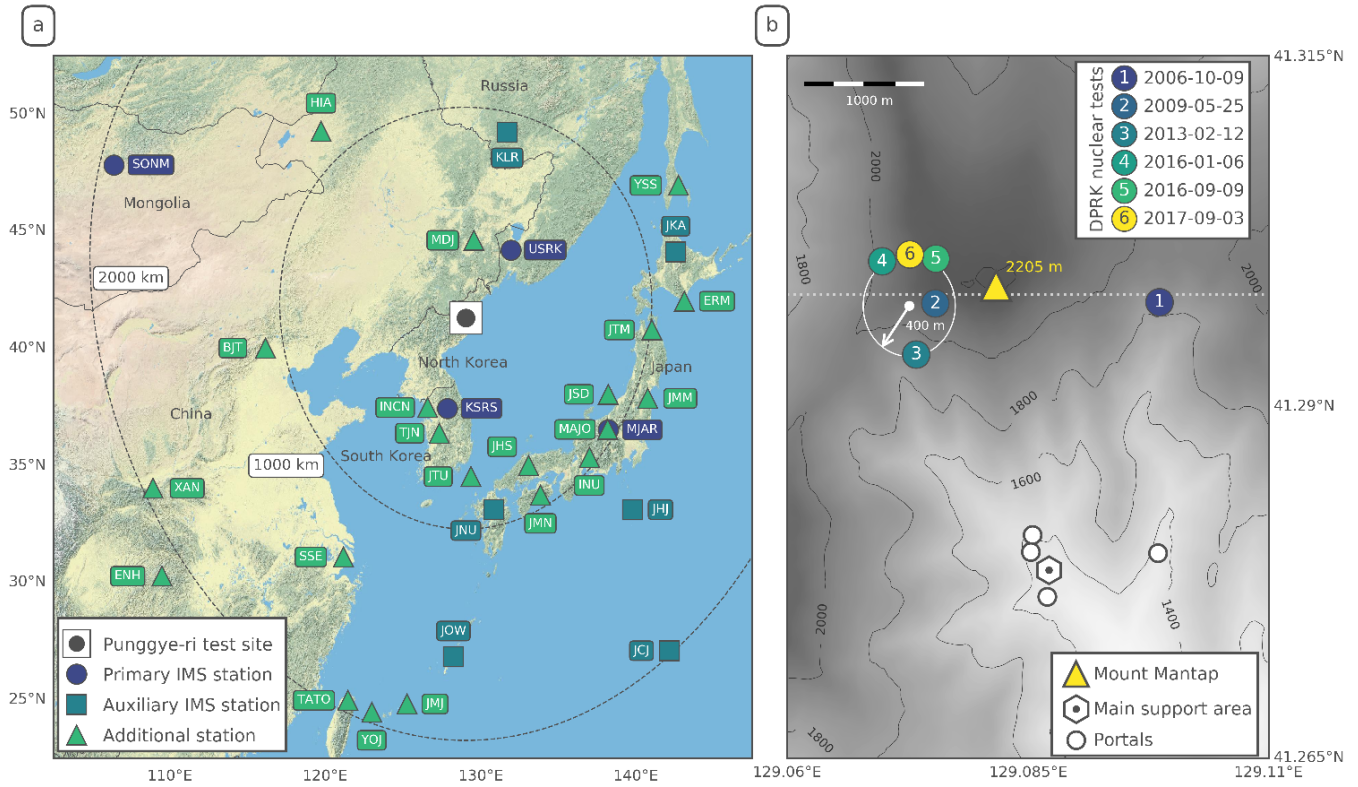


Figure 1. (a) Seismic stations of the International Monitoring System and other earthquake monitoring networks within a radius of 2100 km from the North Korean Punggye-ri nuclear test site. (b) Zoom into the Punggye-ri test site area. Numbered circles indicate the absolute locations of the six North Korean nuclear tests. The relative location error for each test is less than 100 m. Dashed line marks the profile used in Subsection 2.5 to study of topographic influence of the Mt. Mantap on seismic energy generation and radiation from the test.

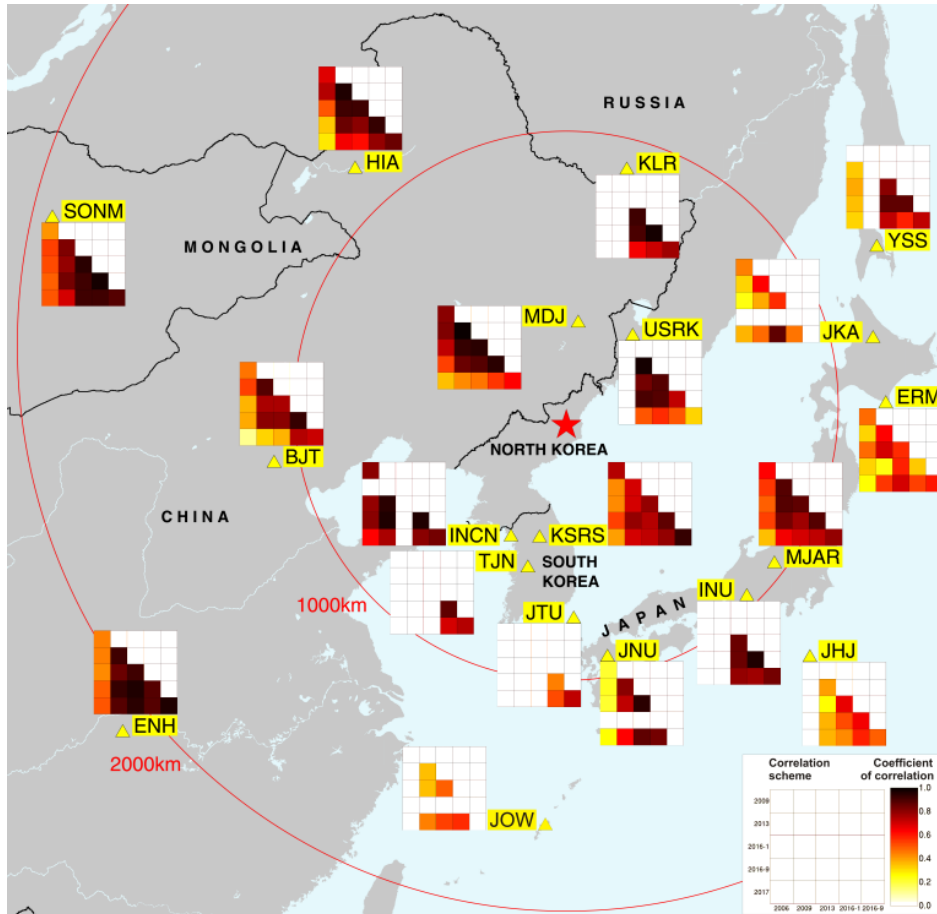


Figure 2. Maximum correlation coefficients for the coherence of the Pn-phase for all available pairs of nuclear tests at 18 stations in regional distances of up to 2100 km. Due to their similar size in explosive yield, the four tests in the years 2009, 2013 and 2016 have a similar source mechanism and consequently show high maximum correlation coefficients between 0.70 and 0.99. The seismic signals for the 2006 and 2017 test are in general less correlated with the other tests due to the different source durations suspected for these two events. The 2006 and 2017 are the smallest and largest explosion, respectively.

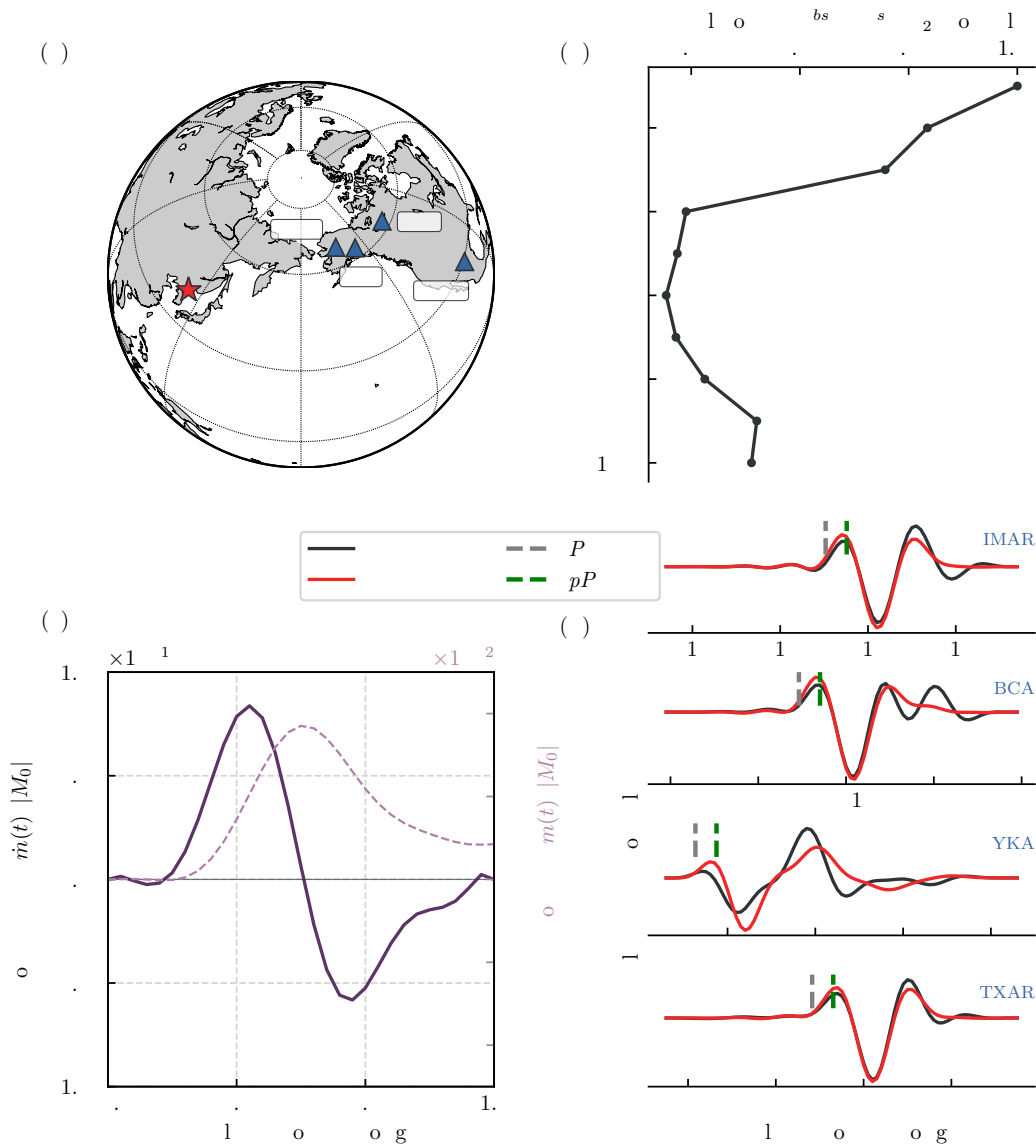


Figure 3. (a) Setup of the depth analysis with the 2017 North Korean nuclear test marked as red star and the four small-aperture, short-period arrays marked as bluish triangles. The epicentral distances to arrays IMAR, BCA, YKA and TXAR are 48° , 54° , 65° and 94° , respectively. (b) Residuals between observed and synthetic waveforms (L_2 -norm) as a function of depth of the explosion. (c) Least squares source time function associated with the best-fit regularized solution. Solid and dashed lines are the normalized moment rate and moment function, respectively. (d) Observed (black) and synthetic (red) waveforms for the best-fit regularized solution at 600 m depth. The gray and green dashed lines indicate the theoretical arrival times of the P- and pP-phases, respectively. The traces are bandpass-filtered between 0.5 and 2.5 Hz.

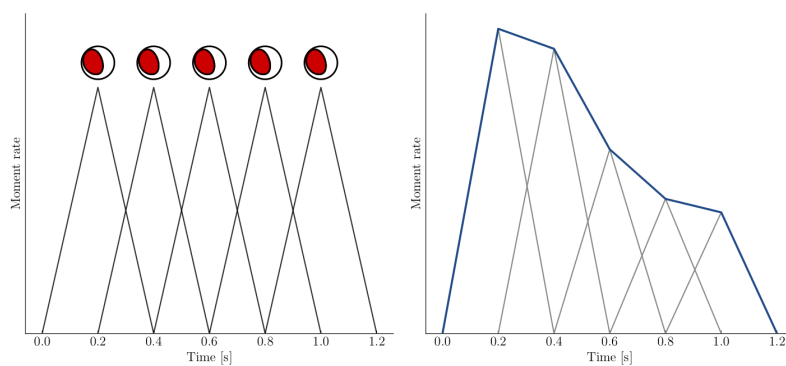


Figure 4. (Left): Schematic sketch of five triangular basis functions $h_i(t)$ with equal weight of 1 and with a duration of 0.4 s each. The focal sphere symbols indicate that the orientation of the source mechanism is assumed constant during the rupture process. (Right): Simulation of a complex moment rate function (blue line) by applying different weights to h_i and linear superposition.

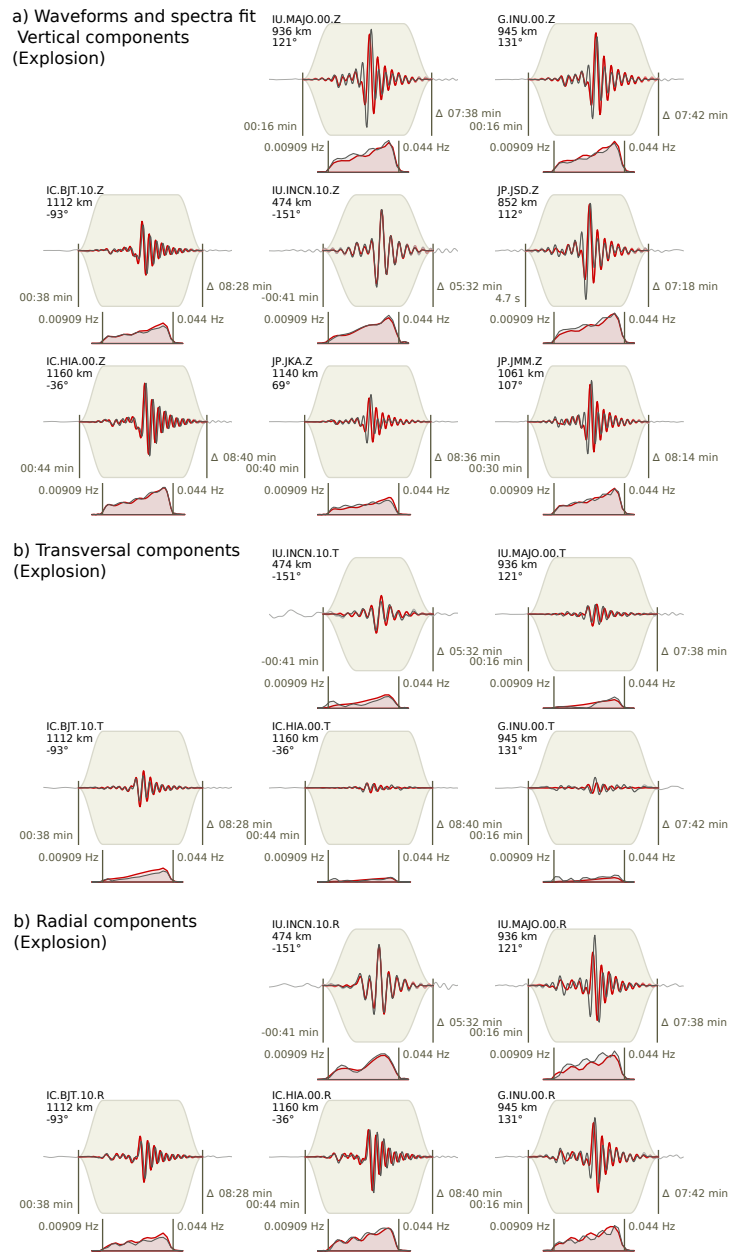


Figure 5. Full waveform displacement and amplitude spectra fits (gray and red lines denote observations and synthetics, respectively) are shown for the nuclear explosion for the vertical (a), transversal (b), and radial components (c). Top left side of each plot reports the trace component (network, station, location, and component codes), epicentral distance, and azimuth. Waveform plots report the starting time (relative to the origin time) and duration (in minutes and seconds) of the time window used (the gray background represents the applied taper), while spectra plots report the frequency range in Hz.

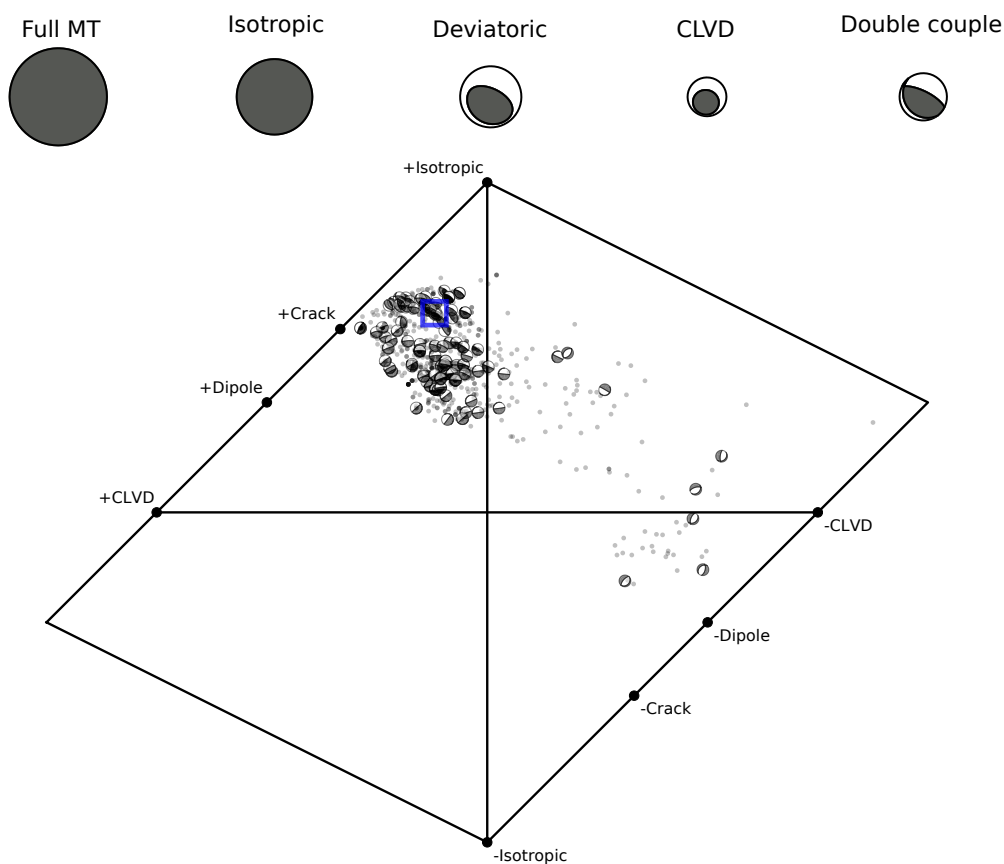
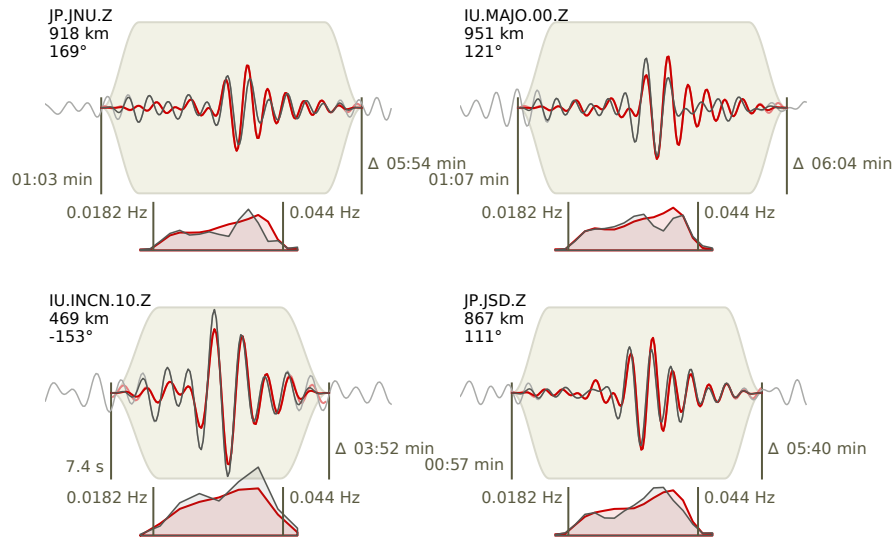


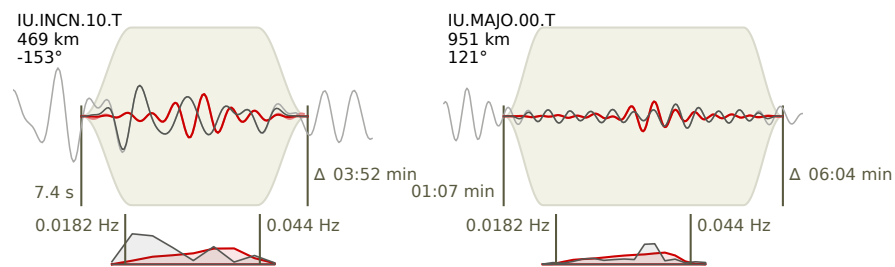
Figure 6. Moment tensor decomposition and source type plots for the 2017 explosion. The moment tensor decompositions report the focal sphere for the full moment tensor, and its isotropic and deviatoric components. The deviatoric component is further decomposed into CLVD and DC terms. The relative size of focal spheres scale with their relative magnitude. The source type diagram after Hudson et al. (1989) is used to judge the moment tensor decomposition, illustrating the ensemble of best fitting solutions. Figure shows both solutions based on all available data, as well as using data subsamples upon bootstrapping (circles, focal spheres for the DC components are shown for selected solutions only). The decomposition of the best solution is denoted by a blue square.



a) Vertical components (Collapse)



b) Transversal components (Collapse)



c) Radial components (Collapse)

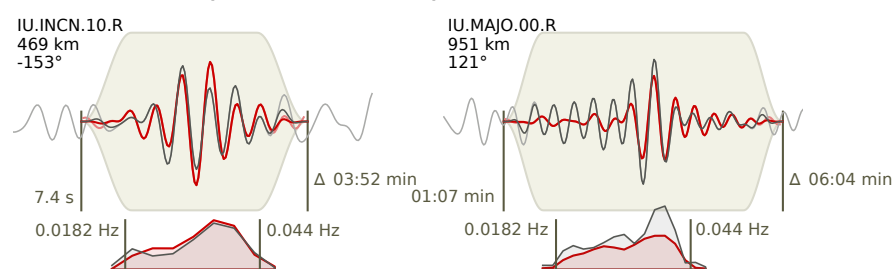


Figure 7. Same as Figure 5, but for the aftershock around eight minutes after the test.

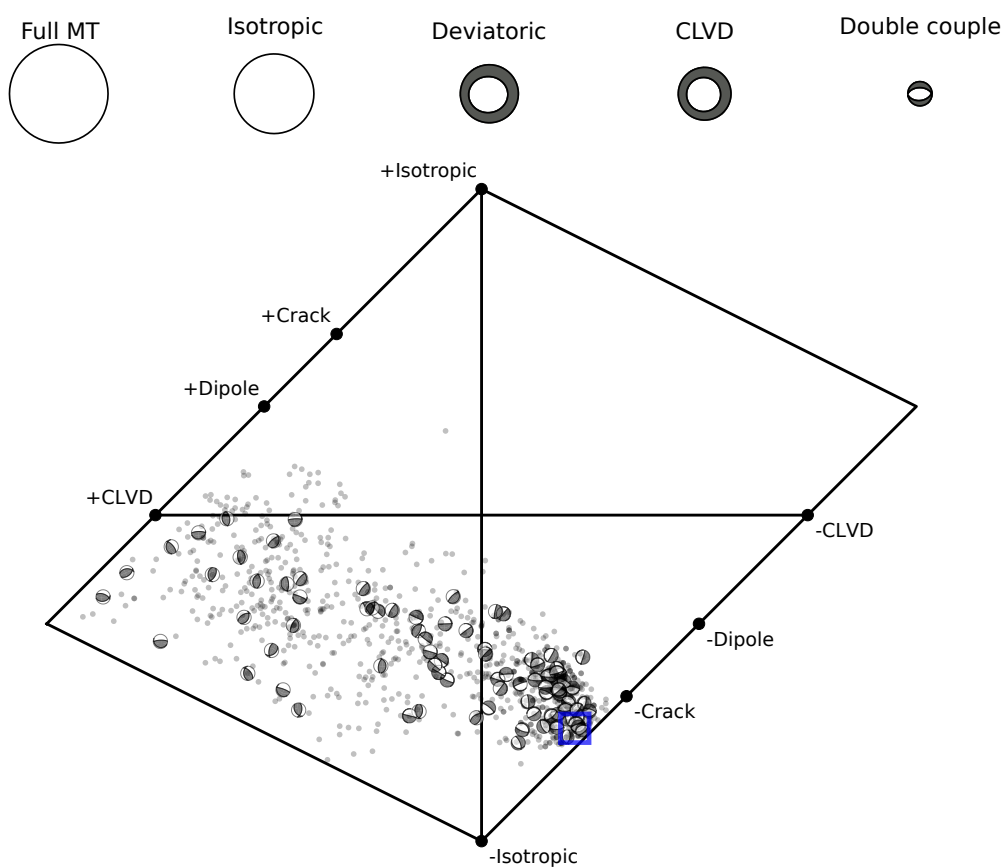


Figure 8. Same as Figure 6, but for the aftershock around eight minutes after the underground test.

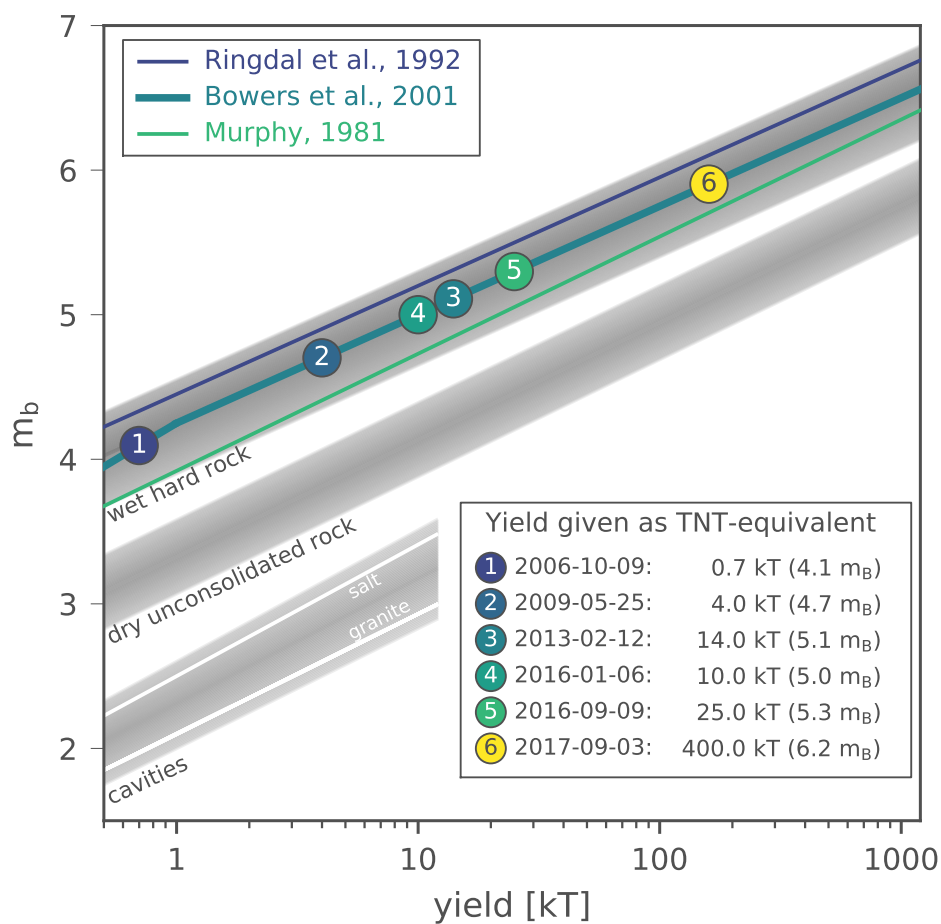


Figure 9. Magnitude-yield relation curves for different geological settings. Numbered circles indicate the six North Korean nuclear tests. Gray background shading represents lower and upper boundary literature values for the different environments.

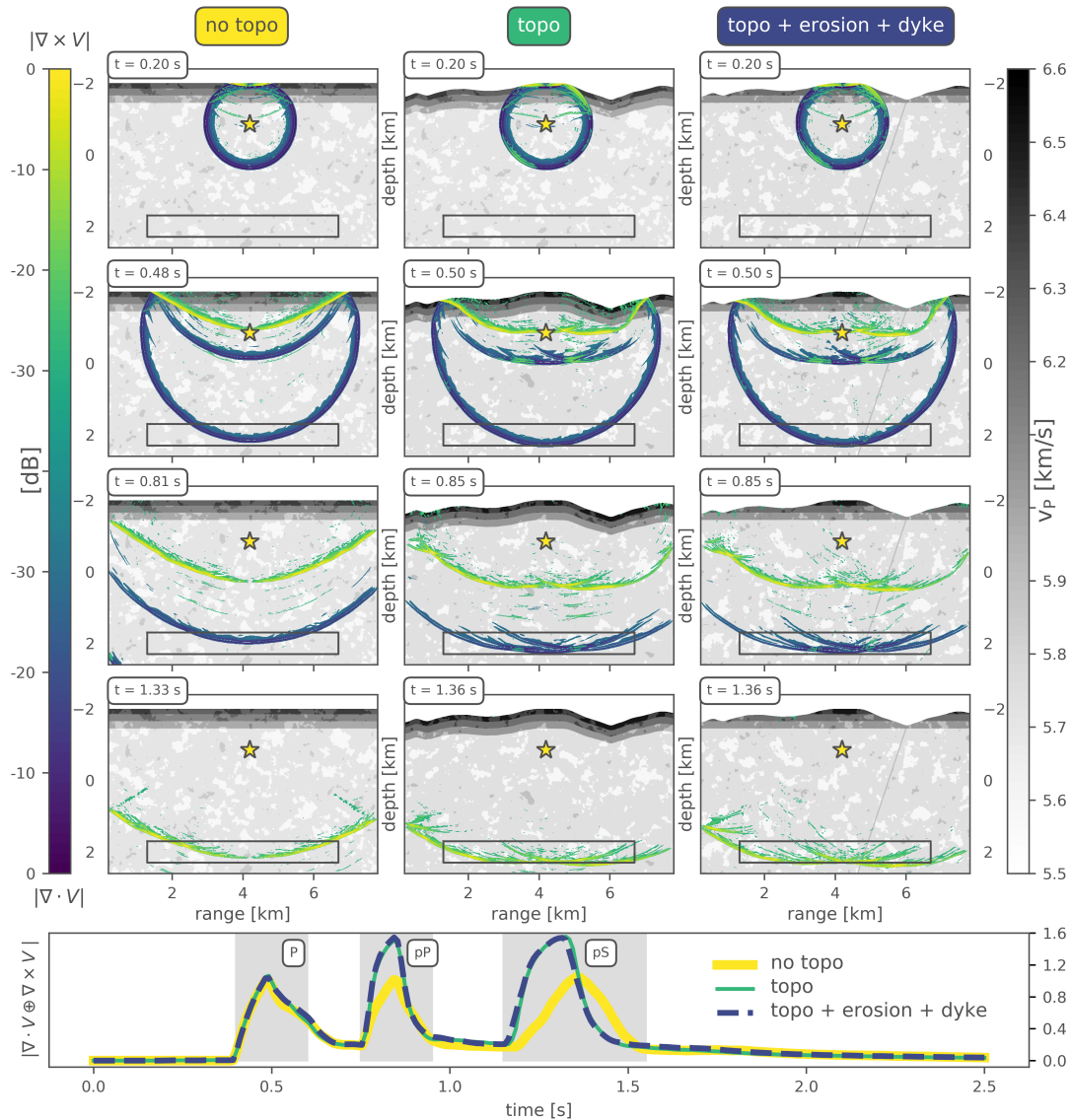


Figure 10. Snapshots obtained by and velocity model used for numerical simulations. P-wave velocities are indicated by shading according to the gray scale map (for S-wave velocities we assume a v_P/v_S -ratio of 1.73), as well as logarithmically scaled divergence (P-wave energy) and curl (SV-wave energy) by bluish and greenish colors, respectively. The left paneled snapshots show the P- and SV-wave separated propagation for an explosion source without topography, the middle panels with topography across the North Korean test site for a West-East profile along 41.3°N with Mt. Mantap in the middle. The right panel shows is similar to the middle panel, but with a more realistic geological setting, where erosion is accounted for. The time stamp of each snapshot is displayed in the upper left corner. The point source is beneath the center of Mt. Mantap in a depth of 0.8 km below surface. The panel below the snapshots compares the summed average divergence and curl computed every 0.02 s in a rectangular box below the source for the case without (yellow) and the cases with (green and blue) topography. The downward propagating wave-field shows strongly increased amplitudes for pP- and pS-phases in both cases of topography.

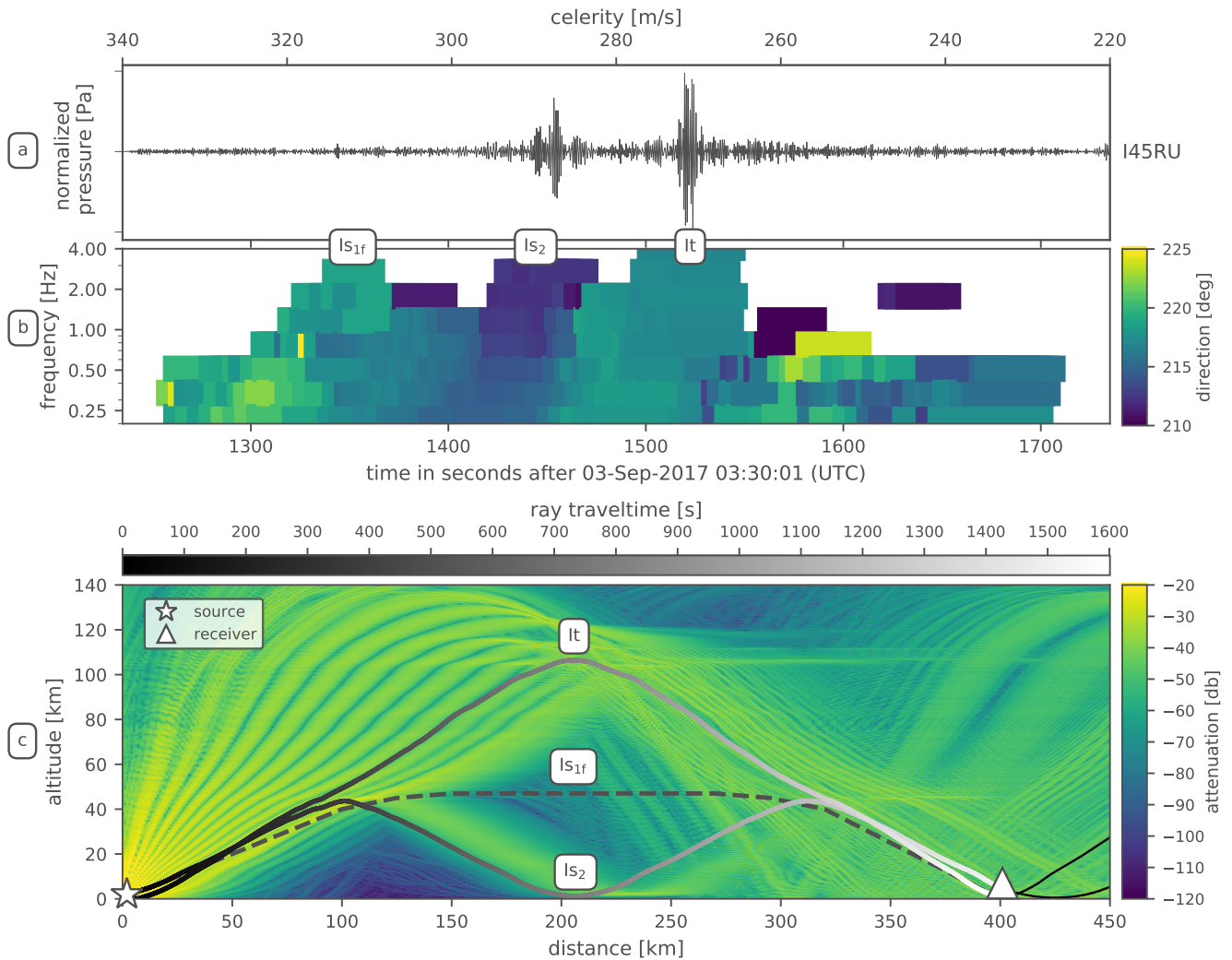


Figure 11. (a) Waveform beam of the 4-element infrasound array I45RU with corresponding celerity values. (b) Progressive Multi-Channel Correlation analysis in the same time frame for signal frequencies between 0.2 and 4 Hz. Information on back-azimuth direction is color coded. True backazimuth from test site to station is 218° . (c) Propagation modeling using raytracing with gray-shaded travel-time information for eigenrays from the test site to the station and color coded attenuation information from parabolic equation modeling. IS_2 and It denote the corresponding stratospheric and thermospheric arrivals. IS_{1f} shows the early signal detection and theoretical raypath for an infrasonic forerunner.

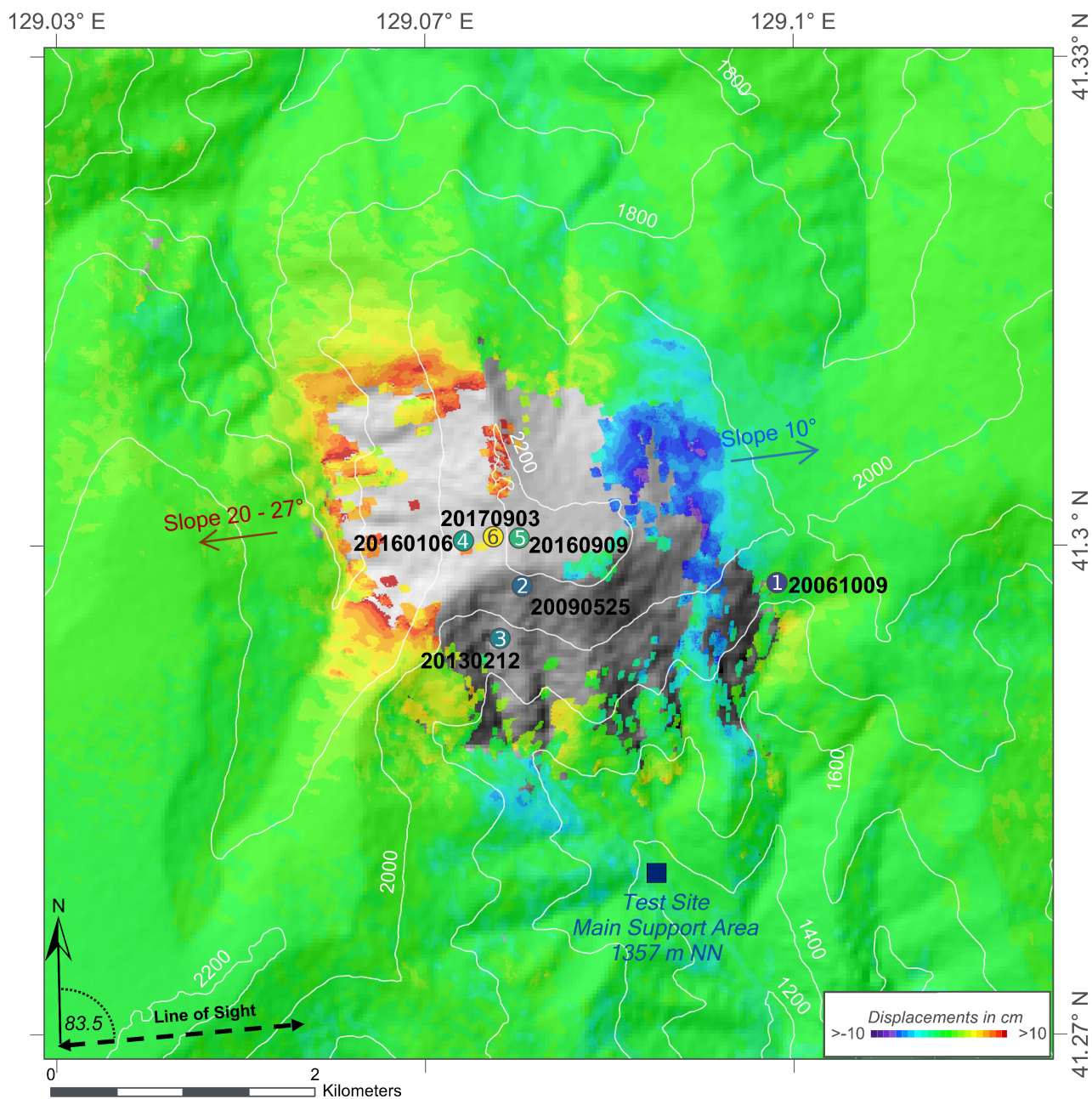


Figure 12. Surface displacements from DINSAR analysis for the 2017 North Korean nuclear test in September 2017. Coherence threshold is set to 0.25. Data from the days August 29th and from September 12th 2017 are used. Arrows indicate slope direction and angle. Numbered circles indicates the epicenters of the tests from 2006 to 2017.

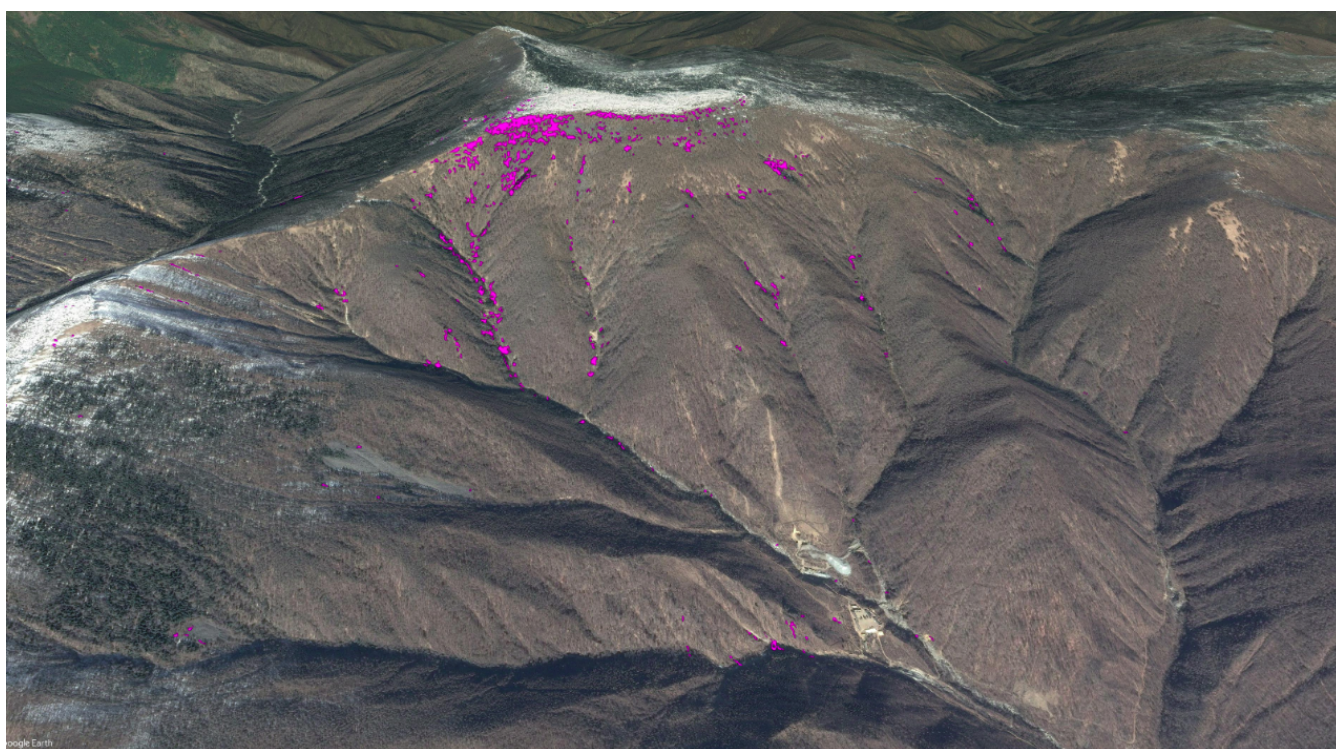


Figure 13. Change detection analyses via NDVI (Normalized Difference Vegetation Index) from Pleiades data showing potential landslides (in purple patches) triggered by the 2017 nuclear test.

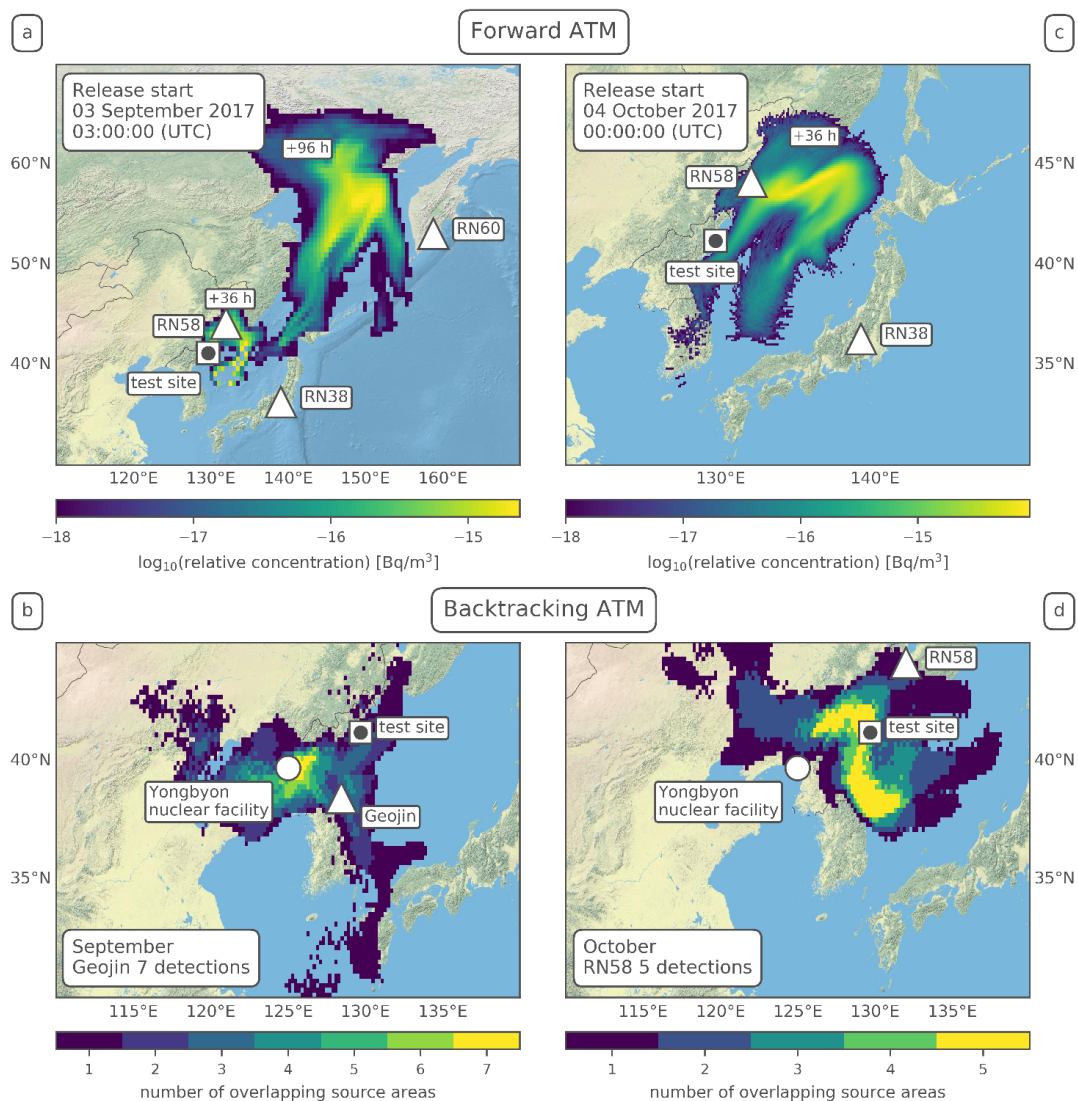


Figure 14. Atmospheric Transport Modeling results. (a) Forward dispersion modeling after 36 and 96 hours for an immediate release on September 3rd 2017. (b) Number of overlapping backward plumes for seven ¹³³Xe detecting samples in north-eastern South Korea from September 7th to 10th 2017 (fixed to 42 hours transport time for each sample). (c) High resolution forward dispersion modeling after 36 hours for a delayed leakage on October 4th 2017. (d) Number of overlapping backward plumes for five ¹³³Xe detecting samples at RN58 Ussuryusk during October 2017 (transport time fixed at maximum sensitivity to North Korean test site).